Geophysical Journal International

Structural properties of the Southern San Andreas fault zone in northern Coachella Valley from magnetotelluric imaging

Journal:	*Geophysical Journal International*
Manuscript ID	GJI-S-21-1108.R1
Manuscript Type:	Research Paper
Date Submitted by the Author:	n/a
Complete List of Authors:	Share, Pieter-Ewald; University of California San Diego Peacock, Jared; US Geological Survey Menlo Park Campus Constable, Steve; Scripps Institution of Oceanography, IGPP Vernon, Frank; IGPP/UCSD Wang, Shunguo; NTNU, ; Uppsala universitet
Keywords:	Electrical properties < GEOMAGNETISM and ELECTROMAGNETISM, Magnetotellurics < GEOMAGNETISM and ELECTROMAGNETISM, Fractures, faults, and high strain deformation zones < TECTONOPHYSICS, Continental tectonics: strike-slip and transform < TECTONOPHYSICS
Additional Keywords:	

Structural properties of the Southern San Andreas fault zone in northern Coachella Valley from magnetotelluric imaging

Pieter-Ewald Share[1*], Jared R. Peacock[2], Steven Constable[1], Frank L. Vernon[1] and Shunguo Wang[3]

[1]Institute of Geophysics and Planetary Physics, University of California San Diego, La Jolla, CA

[2]Geology, Minerals, Energy, and Geophysics Science Center, USGS, Moffett Field, CA

[3]Department of Electronic Systems, Norwegian University of Science and Technology, Trondheim, Norway

[*]Now at College or Earth, Ocean, and Atmospheric Sciences, Oregon State University, Corvallis, OR

Corresponding author: Pieter-Ewald Share (pieter.share@oregonstate.edu)

Geophysical Journal International 2022, in review

Key words: Continental tectonics: strike-slip and transform; Fractures, faults and high strain deformation zones; Electrical properties; Magnetotellurics

Summary

The Southern San Andreas fault (SSAF) poses one of the largest seismic risks in California. Yet, there is much ambiguity regarding its deeper structural properties around Coachella Valley, in large part due to the relative paucity of everyday seismicity. Here, we image a multi-stranded section of the SSAF using a non-seismic method, namely magnetotelluric soundings (MT), to help inform depth-dependent fault zone geometry, fluid content, and porosity. The acquired MT data and resultant inversion models highlight a conductive column encompassing the SSAF zone that includes a 2-3 km wide vertical to steeply northeast dipping conductor down to ~4 km depth (maximum of ~1 Ω.m at 2 km depth) and another prominent conductor in the ductile crust (~1 Ω.m at 12 km depth and slightly southwest of the surface SSAF). We estimate porosities of 18-44% for the conductive uppermost 500 m, 10-15% porosity at 2 km depth and that small amounts (0.1-3%) of highly interconnected saline fluids produce the deeper conductor. Located northeast of this conductive region is mostly resistive crust indicating dry crystalline rock that extends down to ~20 km in places. Most of the local seismicity is associated with this resistive region. Located farther northeast still is a conductive region at >13 km depth and separate from the one in the southwest. The imaged anomalies permit two interpretations. The SSAF zone is vertical to steeply northeast dipping in the upper crust and (1) is near vertical at greater depth creating mostly an impermeable barrier for northeast fluid migration or (2) continues to dip northeast but is relatively dry and resistive up to ~13 km depth where it manifests as a secondary deep ductile crustal conductor. We prefer interpretation (1), but more MT investigations are required.

1. Introduction

The Southern San Andreas Fault (SSAF) has not produced a *M*>7.5 event for >300 years and is estimated to pose one of the largest seismic risks in California (Weldon et al. 2005; Sieh & Williams 1990). Several properties of the SSAF such as fault zone damage, geometry, and fluid content remain poorly understood despite several geoscientific studies (e.g., Catchings et al. 2009; Lindsey & Fialko 2013; Ajala et al. 2019). Informing these properties is essential as they may play key roles in the magnitude and subsequent shaking from future large events (e.g., Roten et al. 2015; Biasi & Wesnousky 2016).

One outstanding question is whether the SSAF at depth, if well localized as expected for a mature plate margin (Montési 2013), is near vertical or dipping to the northeast. In the Southern California Earthquake Center Community Fault Model (SCEC-CFM5.2, Nicholson et al. 2017) it is mapped as a vertical fault in the Coachella Valley (Fig. 1a). In contrast, analyses of interseismic strain fields (Fialko 2006; Tymofyeyeva et al. 2019) and potential field data (Fuis et al. 2012; 2017; Langenheim & Fuis 2021) point to a northeast dipping SSAF similar to its neighboring strand in San Gorgonio Pass (Fig. 1a), the latter being well constrained by small to moderate sized events (Jones et al. 1986; Nicholson 1996). A deep northeast dipping SSAF is supported by more abundant seismicity on that side of the surface SSAF, and a large structure with a prominent seismic velocity contrast (bimaterial interface) intersecting this seismicity (Fig. 1a, Share & Ben-Zion 2016). However, these features can also be attributed to secondary faults in the northeast (Fig. 1a, Nicholson et al. 2017). Much of our inability to resolve this fundamental question about deeper SSAF structure is owed to the general lack of seismicity in the region (Ross et al. 2019), which is essential to delineate fault geometry (e.g., Magistrale & Sanders 1996;

Carena et al. 2004) or in high-resolution seismic imaging studies (e.g., Share et al. 2019). Thus, more studies using non-seismic geophysical tools are needed to help inform SSAF properties and its associated seismic risk.

Here, we use an established electromagnetic imaging method, namely magnetotelluric soundings (MT, Cagnaird 1953), that does not depend on seismicity (or paucity thereof as in the study region) as a source, to image for the first time the electrical resistivity structure of the SSAF throughout the crust. MT is a passive geophysical tool that measures ubiquitous natural variations in the Earth's magnetic field and induced electric fields generated in the subsurface. Resistivity within the Earth is then derived from frequency-dependent transfer functions (MT tensor) between magnetic and electric fields.

MT data are preferentially sensitive to high conductivity (inverse of resistivity) regions within the Earth (Chave & Jones (2012) and references therein). Relative to the deeper mantle continental crust is electrically resistive (Schwarz 1990) except for anomalous regions where conductive materials (e.g., aqueous fluids, graphite, melts) form interconnected networks (e.g., Bahr 1997). Thus, active crustal fault zones are optimal targets for MT imaging, where damaged and deformed rocks create pathways for conductive fluids to percolate through the crust, and strain localization forms a mechanism to connect fluids within these weakened zones (Becken & Ritter 2012). Structure, damage, and deformation need not always be symmetric about a fault core and interconnected fluids can be distributed asymmetrically with little fluid migration across an impermeable fault (e.g., Caine et al. 1996; Bedrosian et al. 2004). MT has been successfully used to infer fault zone properties such as amount of damage, fluid content, geometry, and strain conditions in central California (e.g., Becken et al. 2011; Tietze & Ritter 2013), Japan (Ogawa &

Honkura 2004; Yoshimura et al. 2009) and Turkey (Turkoglu et al. 2008). Despite these successes, MT has yet been broadly applied in Southern California.

In this study, we apply MT imaging to a section of the SSAF in northern Coachella Valley near the Thousand Palms Oasis Preserve where the Mission Creek and Banning fault strands merge (Fig. 1b). Despite ongoing debate over which strand is more active in present day, both are well located at the study site using offsets in landforms and lithology and trenching data (e.g., Fumal et al. 2002; Blisniuk et al. 2021). Near the surface, these strands together with other minor faults comprise a ~3 km wide SSAF zone embedded in Pliocene and Pleistocene stratified rock with Coachella Valley Quaternary sediments to the southwest (up to ~2 km thick in central Valley, Ajala et al. 2019), thinner sediments immediately northeast of the Mission Creek strand and the Little San Bernardino Mountains (pre-Cenozoic metamorphic and crystalline rocks) outcropping ~10 km farther northeast (Rymer 2000). The presence of several oases indicates a fault zone acting as a conduit and/or barrier for aqueous fluid flow (Catchings et al. 2009), making it an attractive MT target. We collected data in 2019 along a linear array transecting the SSAF around the Preserve supplemented by stations from a neighboring 2017-2018 array located in the Joshua Tree National Park (Fig. 1a) to image electric resistivities in the area. The abundant seismicity to the northeast is ~10 km from the Preserve and locates at 4-11 km depth (Fig. 1a). Analyzing MT data that span the SSAF zone and a significant area to the northeast allows us to investigate fault zone resistivities and its connection to local seismicity.

2. Data and Methods

The MT imaging was based on ~1-day long recordings of natural variations in Earth's electromagnetic field at 27 sites crossing the SSAF in 2019 and 6 sites located in Joshua Tree in 2018 (Fig. 1a). These sites were acquired using the Zonge International 32-bit ZEN data logger with ANT-4 magnetic induction coils and Borin Ag-AgCl electrodes with 50 m dipoles. The ZEN was programmed to record in a sequence that started with 256 Hz sampling for 8 hours followed by a burst of 4096 Hz sampling for 10 minutes. This sequence repeated several times within the ~1-day recording window. Accompanying the 2019 survey was a magnetic remote reference installed at a low-noise site in the Borrego Desert (33.271608° N 116.064469° W, ~66 km away). This site consisted of a Scripps marine data logger (Constable 2013) to which a GPS clock had been added, collecting data from two EMI-BF4 induction coils oriented north-south and east-west. Magnetic north was used for orientation during all installations. These recorded continuously at 500 Hz for the duration of the weeklong survey. Given the depths and scale of investigation in this study and that >500 Hz data did not exist for the remote reference site, we excluded the 4096 Hz ZEN data from further analysis. Without a remote reference and with coherent high-frequency noise present across neighboring sites (spaced <500 m near the SSAF), the single-station responses at these very high frequencies may have only yielded biased estimates of near-surface resistivities. To better limit very near-surface properties, water samples from the local oases were collected (Fig. 1b) and their resistivities were measured using a laboratory 4-electrode setup. Both samples had similar measured resistivities of 6.2 Ω.m (18.6°C) and 5.9 Ω.m (18.5°C). Finally, for uniformity, all ZEN data were upsampled to 500 Hz and reformatted to conform to the Scripps marine data format.

Next, recorded time series were inspected and trimmed where needed to remove times with spurious noise. The time series were then transformed to the frequency domain and the frequency coefficients of all stations overlapping in time (including the remote reference) were processed with the code of Egbert (1997) to produce robust MT impedances and induction vectors/tippers (Parkinson 1959). The 500 Hz sampling and the recording period of ~1 day allowed reliable responses to be computed within the ~0.01-2000 s range. The use of the Borrego Desert remote reference significantly improved data quality for some sites.

Following visual inspection of the calculated impedances and tippers, 20% of the impedance data and 16% of the tipper were considered outliers and removed (Fig. 2a). The outliers were generally associated with longest periods (fewer data points per frequency) and southwestern most stations located near the central Coachella Valley where cultural noise was most pronounced (Fig. 2a). This noise affected the electric field recordings more than the magnetic field; thus, tipper data existed at several southwest stations/periods where impedances were otherwise unreliable.

Given the linear nature of the MT array aligned in a southwest-northeast direction where most fault zone structural changes are expected, and the large topographic gradient in the area (22 m to 1495 m), we inverted the responses using the MARE2DEM 2D finite-element algorithm with adaptive meshing that accommodates well irregular topography (Key 2016). Prior to inversion an appropriate strike angle was determined through analyses of the tipper azimuths and phase tensors (Caldwell et al. 2004).

3. Data Analysis

Frequency-dependent phase tensors and tippers provide indicators of the structural characteristics in the area (Figs 2 & S1). Around the Mission Creek strand and shallow depths (<1 s) structure is predominantly 1D, as evidenced by the near circular phase tensors and relatively small tippers. This near surface region probably consists of a shallow layer(s) of damage rock and unconsolidated sediments characteristic of an active fault zone (Blisniuk et al. 2021; Share et al. 2022). After rotating the local coordinate system to the average strike of the Banning and Mission Creek strands (130°/310° E of N, Fig. 1b), the properties of the phase tensor ellipses and tippers show that fault zone geoelectric structures mostly align with fault orientation. At periods ~1-50 s around the Mission Creek strand the phase tensors become elliptical, have <5° beta angles and uniformly align with average fault strike (median strike/alpha=322°, Fig. 2b top). These properties highlight 2D dimensionality at upper to mid crustal depths with geoelectric strike near parallel to average fault strike. This is corroborated by a ~90° flip in beta <5° phase tensor orientations (median strike/alpha=25°, Fig. 2b top) northeast of stations m14-15 (arrow in Figs 1b and 2a), an indication that a prominent fault parallel electric interface has been crossed and the mode with largest phase has flipped from transverse magnetic (TM, southwest conductive side) to transverse electric (TE, northeast resistive side) (Fig. 3). Along the entire profile and for periods up to 50 s, the largest tippers (real part) align with the fault normal (median azimuth=42°/222° E of N, Fig. 2b bottom), further evidence of geoelectric strike approximating fault strike. Moreover, the tippers point (Parkinson convention) toward a region of high conductivity within the SSAF zone (Fig. 2a), most likely related to a fluid-rich region of deformation and damage with the sharp electric contrast around stations m14-15 representing its northeastern edge. At periods >10 s, beta angles start to increase for impedances recorded in the southwest, which may indicate 3D structure but also reflects the noisy nature of these data. Across the array there is a progressive rotation of phase tensor ellipses and tippers at long periods away from average fault strike (or the fault normal), revealing a deep large-scale 3D plate boundary conductor to the northeast (Fig. S1). This rotation starts at lower periods (~5 s) for northeast stations, highlighting again a resistive region with larger skin depth compared to the conductive fault zone. It also causes a median strike angle of 15° less than the fault normal for stations in the northeast (Fig. 2b top). Taken together, the median of all phase tensor strike (alpha) and real tipper angles up to a period of ~50 s (Fig. 2b) defines a coordinate system with X=311.4° (along fault) and Y=41.4° (across fault). Consequently, the impedances and tippers were rotated and >50 s data excluded from 2D modeling as these express 3D features.

4. 2D Inversion

In pseudosections of the rotated data (Fig. 3a), a broad region of high conductivity encompasses the SSAF zone, with average resistivities to the southwest and highest resistivities beneath stations in the northeast. To properly image the area and delineate SSAF structures, we inverted these data using MARE2DEM. The inversion model space consisted of a ~37 km long surface profile with the Mission Creek strand/Thousand Palms Oasis at Y=0 km (Fig. 4) that included local topography (from Smith & Sandwell 1997) and onto which the 33 station locations were projected. Beyond this 37 km profile, topography was set to be flat and extended from Y=-1,000 km to Y=1,000 km. We fixed the resistivity of the air above the surface to 100,000 Ω.m and beneath the surface the initial value was set to 100 Ω.m. The latter extended down to a depth of 1,000 km. From the surface to ~500 m depth beneath the stations the inversion mesh triangles had a target length of 200 m (see Key (2016) for details). Given the dense station spacing (Fig. 1b) and expected high conductivities of an active fault zone (Fig. 3a), we assigned a target length of 500 m to the mesh from Y=-5 km to +5 km and down to 5 km depth. Outside that zone and down to 10 km depth the target length was 1 km, which then gradually increased to 5 km at 50 km depth and 100 km on either side of the 37 km profile. Beyond that the mesh triangles increased without a specified target length to the edges of the model space.

The impedances and tippers of all except the 5 southwestern most stations were assigned error floors of 10% and 0.02, respectively. To the more 3D and/or noisy data in the southwest (Fig. 2a), we assigned error floors of 15% and 0.03. To test the resolution capabilities of these data plus errors, we constructed synthetic tests using hypothetical fault models, data calculated at the same frequencies and locations as the recorded data, and the same inversion mesh (Fig. S2). The test cases all included a 10 Ω.m 2 km wide fault zone but with attitudes varying from a vertical fault zone to one with a shallow dip of 30° to the northeast (Fig. S2). By keeping the fault zone width and resistivity constant these tests demonstrate the variable lateral and depth resolutions of the data and methodology. The resultant inversions (Fig. S2) after adding Gaussian noise of 10% (impedances) and 0.02 (tippers) to the synthetic data suggest the recorded data are well suited to distinguish between these different fault zone geometries.

Next, MARE2DEM was used to invert the recorded data. A target misfit of rms=1 was set at the start of the inversion and a horizontal to vertical smoothing ratio of 0.5 was selected to highlight expected vertical fault related features (Fig. S2). The MARE2DEM algorithm attempts to reach the target misfit as fast as possible and then afterwards determines the smoothest model at that misfit (see Key (2016)). The first inversion was run without inverting for the static shifts produced by shallow small-scale features (e.g., structural heterogeneities, sedimentation/groundwater changes, etc.) and irregular topography. After a few iterations (~5) the inversion was stopped to inspect which of the sites may be affected by static shift. These were identified as sites that had low misfits for TE and TM mode phases and TM mode apparent resistivity but had a parallel shift between the TE mode apparent resistivity data and modeled responses. Of the 33 sites, 17 were identified in this manner as having static shifts. Inversion for static shifts was activated for the 17 sites and the inversion restarted with a homogenous 100 Ω.m subsurface. From a starting rms=9.6, the inversion achieved an rms=1.65 after 13 iterations with only incremental improvements after that. Because the initial target of rms=1 was not reached, the model obtained at rms=1.65 was not necessarily the smoothest for that misfit. So, a new target misfit of rms=1.65 was set and the model after 13 iterations was used as the new starting model, and the inversion restarted. After a total of 18 iterations, the smoothest model (Key 2016) with an rms=1.65 was obtained (Fig. 4). The difference between Figs 3a and 3b, and Fig. S3 illustrate how this misfit maps to the different sites and frequencies.

Three crustal resistivity regions characterize this model. First, a complex region of average to high conductivity (minima of ~1 Ω.m at 2 km depth and 12 km depth, C1&C2) exists in the southwest and terminates at a sharp change in resistivity extending from ~2 km northeast of the surface Mission Creek strand to beneath the Banning strand in the ductile crust. The modeled values in this zone are comparable to those of the central San Andreas fault (Bedrosian et al. 2004; Becken et al. 2011). Second, the crust is mostly resistive northeast of this contrast reaching a maximum of ~10,000 Ω.m in places

(R1&R2). Finally, there exists a conductor, separate from C2, at >13 km depth beneath the most elevated part of the Little San Bernardino Mountains in the Joshua Tree National Park (C3). These features' general characteristics do not change with changes in model smoothing or strike of the 2D profile and associated rotations of data responses (Fig. S4).

Given that some regions in the model space are more poorly resolved than others, such as near surface areas with less station coverage, greater depths in general, and regions beneath conductors (e.g., Chave & Jones 2012), we applied a few conductance-preserving (conductivity-thickness product) alterations of particularly C1-C3 to test if small changes in their properties are allowed without significantly affecting the misfit (i.e., changes within the nullspace, Munoz & Rath 2006). MT data are most sensitive to changes in conductance rather than conductivity, so by preserving conductance these tests highlight how changes in the geometries and locations of C1-C3 affect data misfit. They also provide an indication of their relative influence on misfit and, therefore, the relative data sensitivity to these conductive parts of the model space. In general, the tests show that only small changes in C1-C3 are allowed without significantly increasing the model misfit (Fig. 5). Specifically, the steep northeast dipping geometry of anomaly C1 is well resolved as a more vertically orientated structure in the inverted model increases the rms to ~1.8 (Fig. 5). And, the resistive region separating C2 and C3 is similarly well resolved as extensions of either C2 or C3 towards the other lead to large increases in rms (Fig. 5). For example, extending C2 only 6 km to the northeast produces the same significant increase in rms as removing it from the inverted model altogether (Fig. 5).

The model in Fig. 4 is our preferred result as it is equally well constrained by TE, TM and tipper data (Fig. S3) and the majority of that data at periods <50 s is 2D in nature with a consistent near fault-parallel strike (Fig. 2). However, as noted in Section 3, even at <50 s some stations and periods exhibit 3D characteristics, e.g., at the southwestern and northeastern sites (Fig. 2). As a supplement and to test the effects of these minor 3D features in a predominantly 2D upper to mid crustal region, we additionally applied a 2D determinant inversion (Pedersen & Engels 2005; Wang et al. 2020; 2021). This type of inversion has been shown to produce a less-distorted 2D model representations of a predominantly 2D region that also includes 3D structures (Wang et al. 2020). However, this lower distortion comes at the cost of larger model smoothness. The algorithm employed is embedded in the MARE2DEM package, which facilitates comparison with Fig. 4. During inversion, we used the same impedance tensor data (not tippers), matching errors, and the model and inversion settings described above. Overall, all our resultant determinant inversion models were consistent with Fig. 4. In fact, even when we included data from all available periods, which constituted a significant increase in 3D data, the determinant inversion result was still comparable to Fig. 4 (Fig. S5-S6). In Fig. S5, anomalies C1-3 and R1-2 are all present, albeit the fact that C2 is more conductive and extends to shallower depths, and the region containing R1, R2 and C3 is generally smoother with R1-2 lower in resistivity and C3 smeared towards the northeast where there is less station coverage and the data at longest periods reflect 3D structure (Figs 2 & S1).

As a final reliability test on the inference of a mostly 2D subsurface, a 3D inversion was also carried out using all available data and with the ModEM finite difference code (Kelbert et al. 2014). The features of the 3D model were consistent with our 2D inversions, but lacked the resolution of the MARE2DEM finite element code. These determinant and

3D inversions demonstrate that our 2D modeling approach applied to a limited dataset is justified and features in the resultant 2D model (Fig. 4) can be reliably interpreted.

5. Discussion

Establishing properties related to structure and strain along the SSAF in Coachella Valley is essential for quantifying the potential magnitude and hazard of future large earthquakes. Fault geometrical irregularities play key roles in rupture propagation and subsequently earthquake magnitudes (e.g., Biasi & Wesnousky 2016). Rupture along dipping faults can produce 2-3 times larger ground shaking in the hanging wall compared to the footwall (Fialko 2006). Strain distributed on several neighboring fault strands instead of a primary fault, influences the likelihood of multi-fault rupture and the extent of the resulting ground motion (Lozos 2016).

The results presented here provide insight into these topics as they relate to the SSAF in the northern Coachella Valley (Fig. 4). Anomaly C1 represents the broad SSAF zone (~3 km wide at the surface) in the upper crust. This near-surface width is corroborated by the present of several anomalous fault damage-related structures within that same ~3 km-wide zone as revealed by analysis of large-N seismic array data (Share et al. 2022). It extends to ~4 km depth with largest amplitude at 2 km and locates northeast of the central Coachella Valley, which implies its vertical to steep northeast dip is fault and not Valley basin controlled (Fig 4). If the Banning and Mission Creek strands predominantly constrain C1's geometry, then they likely have similar vertical to northeast dips at upper crustal depths (Catchings et al. 2009; Chi et al. 2021; Langenheim & Fuis 2021). The emergence of conductor C2 at depths >10 km is attributed to the transition from brittle to ductile behavior in the area (Magistrale 2002; Smith-Konter et al. 2011) and a change in pore-space geometry as deep creep causes minute amounts of migrating fluid to become trapped and highly interconnected (Gough 1986; Park et al. 1992; Wannamaker et al. 2008). These deep fluids are likely sourced from the dehydrating metasediments and/or Peninsular Ranges batholith underlying the Coachella Valley sediments. The modelled location of C2 5-10 km southwest of the surface Mission Creek strand has some uncertainty, because of limited station coverage on that side. In contrast, greater station coverage northeast of the Mission Creek results in lower uncertainty and better model resolution and the data do not require C2 to extend significantly in that direction (Fig. 5). Instead, resistor R1 fits the data best and extends near vertically down to ~20 km depth. The high resistivities of R1 suggest relatively dry hard rock, most likely crystalline basement (Catchings et al. 2009; Ajala et al. 2019), and in case these rocks do contain minor conductive materials, then those materials are not well interconnected and/or exist on such a small scale that they are poorly resolved with the MT frequencies employed. Interestingly, most of the seismicity in this area locates within the more resistive parts of the model (Figs 4 & S5) and is closer to conductor C3 than C1 or C2. We propose C3 is a separate fluid or mineral rich creeping zone in the ductile crust that helps drive local earthquake activity in the more resistive and mechanically stronger crust above it. This correlation between smaller scale brittle failure and high resistivity has been observed along minor faults in central California (Bedrosian et al. 2004) and in Turkey (Gurer & Bayrak 2007).

The uppermost 500 m of C1 has an average resistivity of 35 Ω.m (Fig. 4). Assuming the ~6 Ω.m oases samples are representative of the type of fluids reducing the observed resistivities in the shallow fault zone (they interact and react with similar materials) and using Archie's law (Archie 1942), gives porosity estimates of 18% (n=1, highly interconnected crack network) to 44% (n=2, partially connected pores) for the near surface. The further decrease in the resistivity of C1 with depth (minimum of ~1 Ω.m at 2 km depth) can only be explained by decreased fluid resistivities as porosities are expected to decrease with depth also. We suggest two mechanisms driving this. The first is a rapid decrease in fluid resistivity expected in the upper crust due to temperature and pressure increases with depth, which can lead to more than an order of magnitude reduction (Nesbitt 1993). Second, because of the influx of fresh water from the surrounding creeks and mountains, the oases fluids represent an adequate but diluted (more resistive) proxy for the fluids present at 2 km depth in the fault zone. These two factors can result in a reduction of fluid resistivities to <1 Ω.m and produce the observed C1 minimum resistivity if well interconnected cracks with porosities of 10-15% are assumed (e.g., Unsworth et al. 1997; Bedrosian et al. 2004). In the mid-crust porosities decrease even further, the effects of increasing temperature and pressure become negligible (Nesbitt 1993) and observed resistivities are subsequently higher (bottom of C1, Fig. 4). We do not have direct bounds on the conductive material properties producing deeper conductors C2 and C3. Others have suggested that lower crustal conductors in active tectonic settings with resistivities of ~1 Ω.m only require porosities of 0.1-3% if the highly interconnected in situ fluids have salinities close to that of seawater (e.g., Gough 1986; Hyndman et al. 1993; Becken & Ritter 2012). C2 and C3 (at least in part) are likely caused by similar mechanisms.

Taken together, the imaged anomalies and other geophysical inputs permit two interpretations for fault zone geometries and processes (Fig. 4). The major strands of the SSAF zone in the upper crust are vertical to steeply northeast dipping and (1) evolve into a near vertical fault zone at greater depth that acts mostly as a barrier to northeast migration of fluids sourced in the southwest. A mature fault zone with a well-developed core but diminished damage and deformation zones (i.e., SSAF at mid-crustal depths) is likely to be impermeable (Caine et al. 1996). This type of impermeability and asymmetric distribution of crustal fluids about a major transform fault at depth have been observed along, for example, the central San Andreas and the Dead Sea Transform (Ritter et al. 2003; Bedrosian et al. 2004). Consequently, the seismicity in the northeast is associated with secondary or ancestral faults (Fig. 1a) with small (<5%) associated seismic velocity contrasts (Barak et al. 2015; Share & Ben-Zion 2016; Share et al. 2019). This is in line with the SCEC-CFM5.2 and high-resolution geophysical imaging of the same fault strands but 25 km to the northwest (Catchings et al. 2009). Or (2) the SSAF zone continues to dip northeast at greater depth, accommodates some of the local seismicity, manifests as C3 in the ductile crust but is either dry or consists of disconnected small-scale fluid-rich cracks from ~5 to 13 km depth. These characteristics (2) are not indicative of a mature and active transform fault that has probably experienced many large earthquake ruptures (Weldon et al. 2005). And, it requires an alternate explanation for the imaged near vertical crustal resistivity contrast beneath the surface SSAF zone that is not the active plate boundary. However, (2) is consistent with estimates from geodetic (Fialko 2006; Lindsey & Fialko 2013; Tymofyeyeva et al. 2019) and potential field (Fuis et al. 2012; 2017; Langenheim & Fuis 2021) data, the latter being most sensitive to structures at <10 km depth though.

An argument can be made for a non-simple broad deep SSAF zone that is a mix of (1) and (2), but that would require a lack of kilometer-scale localization of ductile fault roots (e.g., Montési 2013) driven by high crustal temperatures and low viscosities (Takeuchi &

Fialko 2013). However, heat flow at the site is on par with well-localized fault systems to the north and west (Lachenbruch et al. 1985; Magistrale 2002) and it only starts increasing farther south, as does the observed shallow creep of the SSAF (Sieh & Williams 1990; Tymofyeyeva et al. 2019). Moreover, the deep crustal conductors imaged in this study, inferred to represent ductile fault roots, are not connected but separated by well-resolved resistive crust (Figs 4, 5, S4 & S5).

6. Conclusions

Our results permit two interpretations of the electric SSAF zone. It is vertical to steeply northeast dipping in the upper crust and (1) is near vertical at greater depth creating mostly an impermeable barrier for northeast fluid migration or (2) continues to dip northeast but is anomalously dry and relatively resistive up to 13 km depth where it manifests as a secondary deep crustal conductor. We prefer the deeper near vertical fault interpretation (1) as it is the simplest explanation for the active SSAF zone. It is also consistent with other major transform fault systems both in terms of resistivity and its complex shallow to simpler deeper fault zone nature. In any case, the general lack of seismicity and presence of shallow aseismic creep along parts of the Coachella Valley SSAF remain enigmatic. More insights from MT and other geophysical tools are required including joint inversions, which is beyond the scope of this focused study. As a start, we suggest several new across-fault MT arrays in the area. To the southeast these will help establish the along-strike continuity of anomalies C1-C3 and R1, respectively, and delineate changing fault zone widths, geometries, and their connection to seismicity, heat flow and creep. To the northwest more MT data will illuminate the large-scale 3D conductor identified in Figs 2a & S1 and its relation to regional tectonics.

Acknowledgements

We thank Deborah Rogers and Ginny Short (Center for Natural Lands Management and Thousand Palms Oasis Preserve), Brian Ousley (Bureau of Land Management), Tom Anderson, Chris Schoneman and Alicia Thomas (Sonny Bono Salton Sea National Wildlife Refuge), and Martin Alvarez (City of Palm Desert) for help with permitting and access to the field sites. We also acknowledge graduate students Hannah Peterson and Rosslyn King for their assistance during field work. We thank Kerry Key and Gary Egbert for their analysis codes, and Yuri Fialko, Rasheed Ajala and Victoria Langenheim for useful discussions. This work was supported by the Southern California Earthquake Center (SCEC) Award #19200. P.-E. Share was also supported by a Green Foundation Postdoctoral Fellowship (Institute of Geophysics and Planetary Physics/Scripps Institution of Oceanography). S.Wang was funded by the Norwegian Research Council (294404, 309960, and 324442) and the National Infrastructure for High-Performance Computing and Data Storage in Norway (nn9872k).

Data Availability

All data are publicly available through ScienceBase (https://doi.org/10.5066/P990U7GE).

References

Ajala, R., Persaud, P., Stock, J. M., Fuis, G. S., Hole, J. A., Goldman, M. R., & Scheirer, D. S. (2019). Three-dimensional basin and fault structure from a detailed seismic velocity model of Coachella Valley, Southern California. Journal of Geophysical Research, 124(5), 4728-4750.

Archie, G. E. (1942). The Electrical Resistivity Log as an Aid in Determining Some Reservoir Characteristics. Transactions of the AIME, 146(01), 54–62. https://doi.org/10.2118/942054-G

Bahr, K. (1997). Electrical anisotropy and conductivity distribution functions of fractal random networks and of the crust: the scale effect of connectivity. Geophysical Journal International, 130, 649-660.

Barak, S., Klemperer, S. L., & Lawrence, J. F. (2015). San Andreas Fault dip, Peninsular Ranges mafic lower crust and partial melt in the Salton Trough, Southern California, from ambient-noise tomography. Geochemistry Geophysics Geosystems, 16, 3946-3972.

Becken, M., & Ritter, O. (2012). Magnetotelluric studies at the San Andreas Fault Zone: Implications for the role of fluids. Surveys in Geophysics, 33(1), 65-105.

Becken, M., Ritter, O., Bedrosian, P. A., & Weckmann, U. (2011). Correlation between deep fluids, tremor and creep along the central San Andreas Fault. Nature, 480(7375), 87-90.

Bedrosian, P. A., Unsworth, M. J., Egbert, G. D., & Thurber, C. H. (2004). Geophysical images of the creeping segment of the San Andreas Fault: implications for the role of crustal fluids in the earthquake process. Tectonophysics, 385, 137-156.

Biasi, G. P., & Wesnousky, S. G. (2016). Steps and Gaps in Ground Ruptures: Empirical Bounds on Rupture Propagation. *Bulletin of the Seismological Society of America*, *106*(3), 1110–1124. https://doi.org/10.1785/0120150175

Blisniuk, K., Scharer, K., Sharp, W. D., Burgmann, R., Amos, C., & Rymer, M. (2021). A revised position for the primary strand of the Pleistocene-Holocene San Andreas fault in southern California. *Science Advances*, *7*(13), eaaz5691. https://doi.org/10.1126/sciadv.aaz5691

Cagniard, L. (1953). Basic theory of the magneto-telluric method of geophysical prospecting. Geophysics, 18, 605-635.

Caine, J.S., Evans, J.P., & Forster, C.B. (1996). Fault zone architecture and permeability structure. Geology 24, 1025–1028.

Caldwell, T. G., Bibby, H. M., & Brown, C. (2004). The magnetotelluric phase tensor. Geophysical Journal International, 158, 457-469.

Carena, S., Suppe, J., & Kao, H. (2004). Lack of continuity of the San Andreas Fault in southern California: Three-dimensional fault models and earthquake scenarios. *Journal of Geophysical Research: Solid Earth*, *109*(B4). https://doi.org/https://doi.org/10.1029/2003JB002643

Catchings, R. D., Rymer, M. J., Goldman, M. R., & Gandhok, G. (2009). San Andreas Fault Geometry at Desert Hot Springs, California, and Its Effects on Earthquake Hazards and Groundwater. *Bulletin of the Seismological Society of America*, *99*(4), 2190–2207. https://doi.org/10.1785/0120080117

Chave, A. D., & Jones, A. G. (Eds.) (2012). *The Magnetotelluric Method: Theory and Practice*. Cambridge University Press. 552 pp.

Chi, B., Qiu, H., Share, P.-E., Vernon, F. L., & Ben-Zion, Y. (2021). Reverse-time migration of fault zone reflected waves: Methodology and application to the Southern San Andreas fault. Seismological Research Letters, 92 (2B), 1422. https://doi.org/10.1785/0220210025

Constable, S. (2013). Review paper: Instrumentation for marine magnetotelluric and controlled source electromagnetic sounding. *Geophysical Prospecting*, *61*(s1), 505–532. https://doi.org/https://doi.org/10.1111/j.1365-2478.2012.01117.x

Egbert, G. D. (1997). Robust multiple-station magnetotelluric data processing. Geophysical Journal International, 130, 475-496.

Fialko, Y. (2006). Interseismic strain accumulation and the earthquake potential on the southern San Andreas fault system. *Nature*, *441*(7096), 968–971. https://doi.org/10.1038/nature04797

Fuis, G. S., Scheirer, D. S., Langenheim, V. E., & Kohler, M. D. (2012). A new perspective on the geometry of the San Andreas fault in southern California and its relationship to lithospheric structure. Bulletin of the Seismological Society of America, 102(1), 236-251.

Fuis, G. S., Bauer, K., Goldman, M. R., Ryberg, T., Langenheim, V. E., Scheirer, D. S., Rymer, M. J., Stock, J. M., Hole, J. A., Catchings, R. D., Graves, R. W., & Aagaard, B. (2017). Subsurface geometry of the San Andreas Fault in Southern California:

Results from the Salton Seismic Imaging Project (SSIP) and strong ground motion expectations. Bulletin of the Seismological Society of America, 107(3), 1642-1662.

Fumal, T. E., Rymer, M. J., & Seitz, G. G. (2002). Timing of Large Earthquakes since A.D. 800 on the Mission Creek Strand of the San Andreas Fault Zone at Thousand Palms Oasis, near Palm Springs, California. *Bulletin of the Seismological Society of America*, *92*(7), 2841–2860. https://doi.org/10.1785/0120000609

Gough, D. I. (1986). Seismic reflectors, conductivity, water and stress in the continental crust. Nature, 323, 143-144.

Gurer, A., & Bayrak, M (2007). Relation between electrical resistivity and earthquake generation in the crust of West Anatolia, Turkey. Tectonphysics, 445, 49-65.

Hyndman, R. D., Vanyan, L. L., Marquis, G., & Law, L. K. (1993). The origin of electrically conductive lower continental crust: saline water or graphite? Physics of the Earth and Planetary Interiors, 81(1), 325–345.

Jones, L. M., Hutton, L. K., Given, D. D., & Allen, C. R. (1986). The North Palm Springs, California, earthquake sequence of July 1986, *Bulletin of the Seismological Society of America*, 76, 1830–1837.

Kelbert, A., Meqbel, N., Egbert, G. D., & Tandon, K. (2014). ModEM: A modular system for inversion of electromagnetic geophysical data. Computers & Geosciences, 66, 40–53. https://doi.org/https://doi.org/10.1016/j.cageo.2014.01.010

Key, K. (2016). MARE2DEM: a 2-D inversion code for controlled-source electromagnetic and magnetotelluric data. Geophysical Journal International, 207(1), 571-588.

Lachenbruch, A. H., Sass, J. H., & Galanis Jr., S. P. (1985). Heat flow in southernmost California and the origin of the Salton Trough. *Journal of Geophysical Research: Solid Earth*, *90*(B8), 6709–6736. https://doi.org/10.1029/JB090iB08p06709

Langenheim, V. E., & Fuis, G. S. (2022). Insights into the geometry and evolution of the southern San Andreas fault from geophysical data, southern California. *Geosphere*, *18*(2), 458–475.

Lindsey, E. O., & Fialko, Y. (2013). Geodetic slip rates in the southern San Andreas Fault system: Effects of elastic heterogeneity and fault geometry. Journal of Geophysical Research, 118, 689-697.

Lozos, J. C. (2016). A case for historic joint rupture of the San Andreas and San Jacinto faults. Science Advances, 2(3), e1500621.

Magistrale, H., & Sanders, C. (1996), Evidence from precise earthquake hypocenters for segmentation of the San Andreas fault in San Gorgonio Pass, Journal of Geophysical Research, 101, 3031-3044.

Magistrale, H. (2002). Relative contributions of crustal temperature and composition to controlling the depth of earthquakes in Southern California. Geophysical Research Letters, 29(10), 1447.

Montési, L. G. J. (2013). Fabric development as the key for forming ductile shear zones and enabling plate tectonics. *Journal of Structural Geology*, *50*, 254–266.

Muñoz, G., & Rath, V. (2006). Beyond smooth inversion: the use of nullspace projection for the exploration of non-uniqueness in MT. *Geophysical Journal International*, *164*(2), 301–311.

Nesbitt, B. E. (1993). Electrical resistivities of crustal fluids. Journal of Geophysical Research, 98(B3), 4301-4310.

Nicholson, C. (1996). Seismic behavior of the southern San Andreas fault zone in the northern Coachella Valley, California: Comparison of the 1948 and 1986 earthquake sequences, *Bulletin of the Seismological Society of America*, 86, 1331–1349.

Nicholson, C., A. Plesch and J.H. Shaw (2017). Community Fault Model Version 5.2: Updating & expanding the CFM 3D fault set and its associated fault database, *2017 SCEC Annual Meeting Proceedings & Abstracts*, XXVII, poster 234, p.142-143.

Ogawa, Y., & Honkura, Y. (2004). Mid-crustal electrical conductors and their correlations to seismicity and deformation at Itoigawa-Shizuoka tectonic line, Central Japan. Earth Planets Space, 56, 1285-1291.

Park, S. K., Jiracek, G. R., & Johnson, K. M. (1992). Magnetotelluric evidence for a brittle-ductile transition, peninsular ranges batholith, southern California? *Geophysical Research Letters*, *19*(21), 2143–2146. https://doi.org/10.1029/92GL02439

Parkinson, W. D. (1959). Directions of rapid geomagnetic fluctuations. Geophysical Journal of the Royal Astronomical Society, 2(1), 1-14.

Pedersen, L. B., & Engels, M. (2005). Routine 2D inversion of magnetotelluric data using the determinant of the impedance tensor. *GEOPHYSICS*, *70*(2), G33–G41.

Ritter, O., Weckmann, U., Hoffmann-Rothe, A., Abueladas, A., Garfunkel, Z., & DESERT Research Group (2003). Geophysical images of the Dead Sea Transform in Jordan reveal an impermeable barrier for fluid flow. Geophysical Research Letters, 30. https://doi.org/10.1029/2003GL017541

Roten, D., Olsen, K. B., Cui, Y. & Day, S. M., 2015. Quantification of fault zone plasticity effects with spontaneous rupture simulations, in *Best Practices in Physics-based Fault Rupture Models for Seismic Hazard Assessment of Nuclear Installations*, Vienna, Austria.

Ross, Z. E., Trugman, D. T., Hauksson, E. & Shearer, P., (2019). Searching for hidden earthquakes in Southern California, Science, 364(6442), 767-771.

Rymer, M. J. (2000). Triggered Surface Slips in the Coachella Valley Area Associated with the 1992 Joshua Tree and Landers, California, Earthquakes. *Bulletin of the Seismological Society of America*, *90*(4), 832–848. https://doi.org/10.1785/0119980130

Schwarz, G. (1990). Electrical conductivity of the earth's crust and upper mantle. Surveys in Geophysics, 11, 133-161.

Share, P.-E., & Ben-Zion, Y. (2016). Bimaterial interfaces in the South San Andreas Fault with opposite velocity contrasts NW and SE from San Gorgonio Pass. Geophysical Research Letters, 43(20), 10680-10687.

Share, P.-E., Guo, H., Thurber, C. H., Zhang, H. & Ben-Zion, Y., 2019. Seismic imaging of the Southern California plate-boundary around the South-Central Transverse Ranges using double-difference tomography, Pure and Applied Geophysics, 176(3), 1117-1143.

Share, P., Qiu, H., Vernon, F. L., Allam, A. A., Fialko, Y., & Ben-Zion, Y. (2022). General Seismic Architecture of the Southern San Andreas Fault Zone around the Thousand Palms Oasis from a Large-N Nodal Array. *The Seismic Record*, *2*(1), 50–58.

Sieh, K., & Williams, P. (1990). Behavior of the southernmost San Andreas fault during the past 300 years. *Journal of Geophysical Research*, 95, 6629–6645.

Smith, W. H. F., & Sandwell, D. T. (1997). Global seafloor topography from satellite altimetry and ship depth soundings. *Science*, 277, 1957–1962.

Smith-Konter, B. R., Sandwell, D. T., & Shearer, P. (2011). Locking depths estimated from geodesy and seismology along the San Andreas Fault System: Implication for seismic moment release. Journal of Geophysical Research, 116, B06401.

Takeuchi, C. S., & Fialko, Y. (2013). On the effects of thermally weakened ductile shear zones on postseismic deformation. *Journal of Geophysical Research: Solid Earth*, *118*(12), 6295–6310. https://doi.org/https://doi.org/10.1002/2013JB010215

Tietze, K., & Ritter, O. (2013). Three-dimensional magnetotelluric inversion in practice—the electrical conductivity structure of the San Andreas Fault in Central California. *Geophysical Journal International*, *195*(1), 130–147. https://doi.org/10.1093/gji/ggt234

Turkoglu, E., Unsworth, M., Caglar, I., Tuncer, V., & Avsar, U. (2008). Lithospheric structure of the Arabia-Eurasia collision zone in eastern Anatolia: magnetotelluric evidence for widespread weakening by fluids? Geology, 36, 619-622.

Tymofyeyeva, E., Fialko, Y., Jiang, J., Xu, X., Sandwell, D., Bilham, R., Rockwell, T. K., Blanton, C., Burkett, F., Gontz, A., & Moafipoor, S. (2019). Slow slip event on the southern San Andreas fault triggered by the 2017 M_W8.2 Chiapas (Mexico) earthquake. *Journal of Geophysical Research*, 124, B016765.

Unsworth, M. J., Malin, P. E., Egbert, G. D., & Booker, J. R. (1997). Internal structure of the San Andreas fault at Parkfield, California. Geology, 25(4), 359–362.

Wang, S., Constable, S., Reyes-Ortega, V, Jahandari, H., Farquharson, C., & Avile-Esquivel, T. (2020). Two-dimensional determinant inversion of marine magnetotelluric data and a field example from the Gulf of California, Mexico. *Geophysics*, 86, E37–E57.

Wang, S., Constable, S., Rychert, C. A., & Harmon, N. (2021). A lithosphere-asthenosphere boundary and partial melt resolved using marine magnetotelluric data, *Geochemistry Geophysics Geosystems,* 21, doi.org/10.1029/2020GC009177

Wannamaker, P. E., Hasterok, D. P., Johnston, J. M., Stodt, J. A., Hall, D. B., Sodergren, T. L., Pellerin, L., Maris, V., Doerner, W. M., Groenewold, K. A., & Unsworth, M. J. (2008). Lithospheric dismemberment and magmatic processes of the Great Basin-Colorado Plateau transition, Utah, implied from magnetotellurics, Geosystems Geophysics Geochemistry, 9, Q05019.

Weldon, R. J., Fumal, T. E., Biasi, G. P., Scharer, K. M. (2005). Past and future earthquakes on the San Andreas fault, Science, 308, 966-967.

Yoshimura, R., Oshiman, N., Uyeshima, M., Toh, H., Uto, T., Kanezaki, H., Mochido, Y., Aizawa, K., Ogawa, Y., Nishitani, T., Sakanaka, S., Mishina, M., Satoh, H., Goto, T., Kasaya, T., Yamaguchi, S., Murakami, H., Mogi, T., Yamaya, Y., Harada, M., Shiozaki, I., Honkura, Y., Koyama, S., Nakao, S., Wada, Y., & Fujita, Y. (2009). Magnetotelluric transect across the niigata-kobe tectonic zone, central Japan: a clear correlation between strain accumulation and resistivity structure. Geophysical Research Letters, 36, L20311.

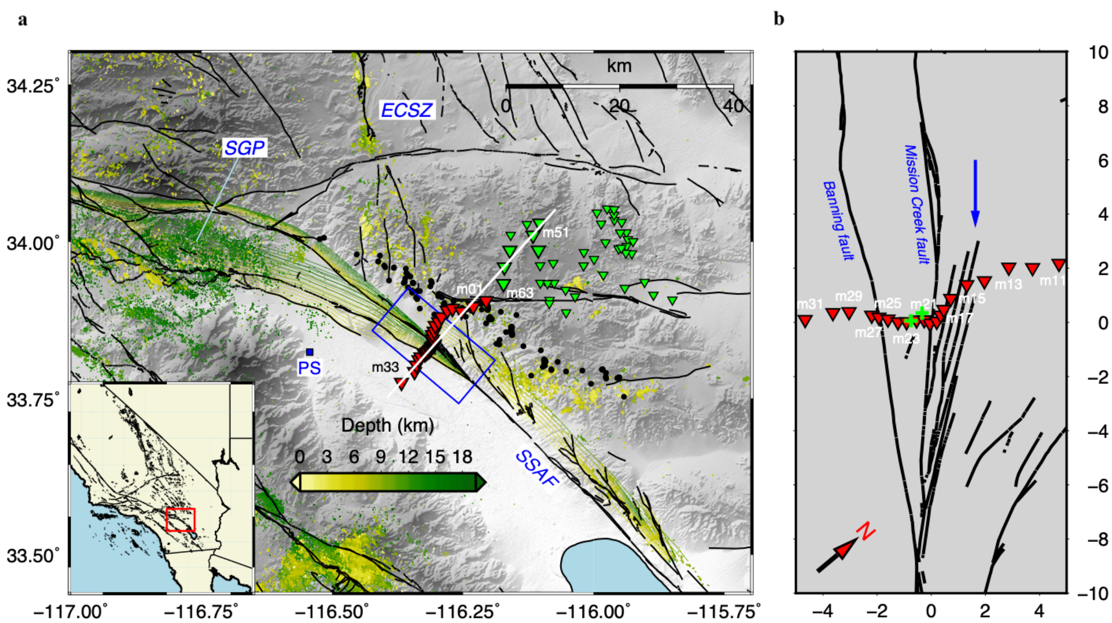

Figure 1: Study area in the context of the Southern San Andreas Fault (SSAF). (a) Fault traces at the surface (black lines) and contours along the SSAF planes from shallow (yellow) to 14 km depth (green) from the SCEC-CFM5.2 (see text). The SSAF strand accommodating most of the plate boundary strain to the south is estimated to be vertical and has no contours. Secondary or ancestral faults are associated with the dipping structures (contours) to the northeast. Magnetotelluric (MT) stations acquired in 2019 (red) and in the Joshua Tree National Park during 2017-2018 (green) are depicted by triangles. Larger triangles show stations used in the 2D inversion and the white line represents the inversion model transect in Fig. 4. Depth colored dots are local earthquakes from the Ross et al. (2019) catalog. Black dots are events illuminating a large bimaterial structure at depth. Note the relative lack of seismicity directly beneath the SSAF and especially near the study area.

San Gorgonio Pass (SGP), the Eastern California Shear Zone (ECSZ) and the town of Palm Springs (PS) are shown for reference. (b) Zoom in of blue box in (a) showing the MT profile transecting the SSAF zone, which consists of the Banning, Mission Creek, and other minor fault strands. The blue arrow shows the location of a large change in electric resistivity in the across-fault direction (same arrow appears in Figs 2-4). The Thousand Palms Oasis Preserve Visitor Center is located at the origin and the green crosses show the locations of two fluid samples taken from the oases.

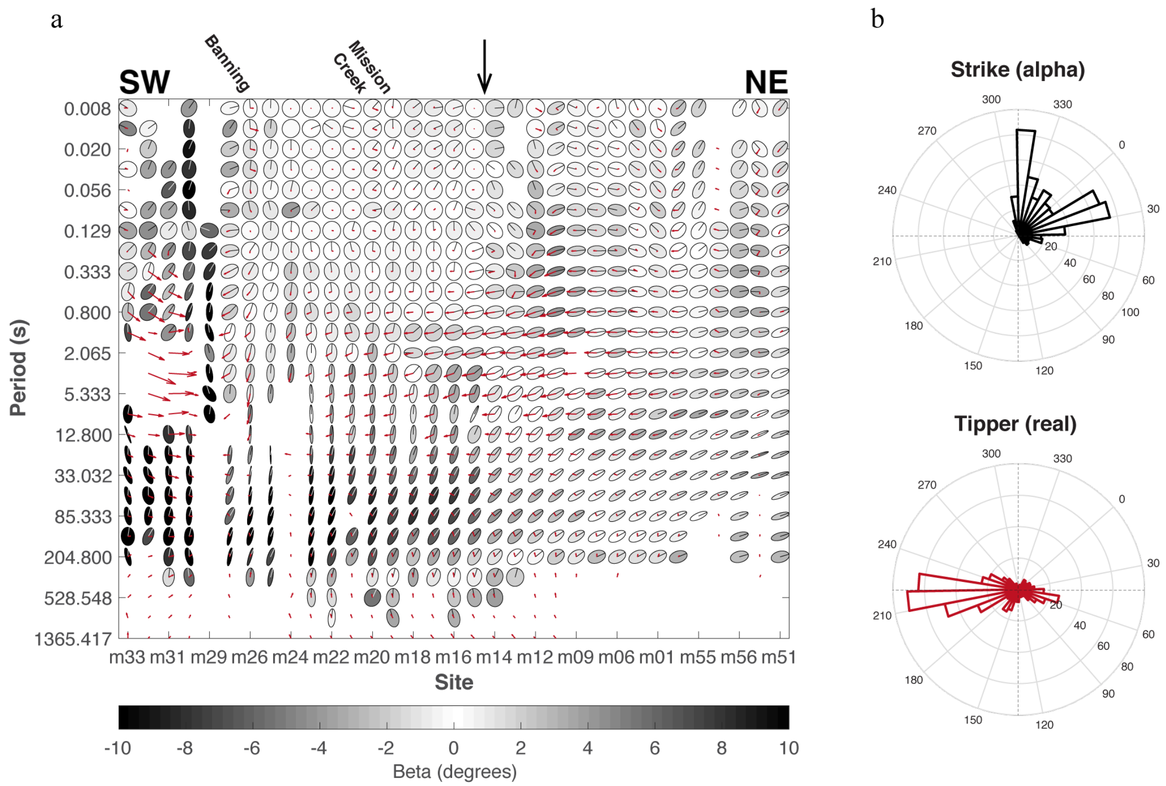

Figure 2: Phase tensor and tipper results. (a) Phase tensor ellipses and real tipper vectors (maroon arrows, Parkinson convention) of all data after outliers (gaps) were removed. The degree of ellipticity equals the difference between Phi-min and Phi-max, the black lines inside ellipses point to calculated strike (alpha) and the orientation of the major axes of ellipses relative to strike and the shading of the ellipses equals beta. The coordinate frame is the same as in Fig. 1b. (b) Histograms of strike (top) and real tipper azimuths (bottom) for data up to 50 s. The dashed lines show the coordinate frame used (same as in (a)).

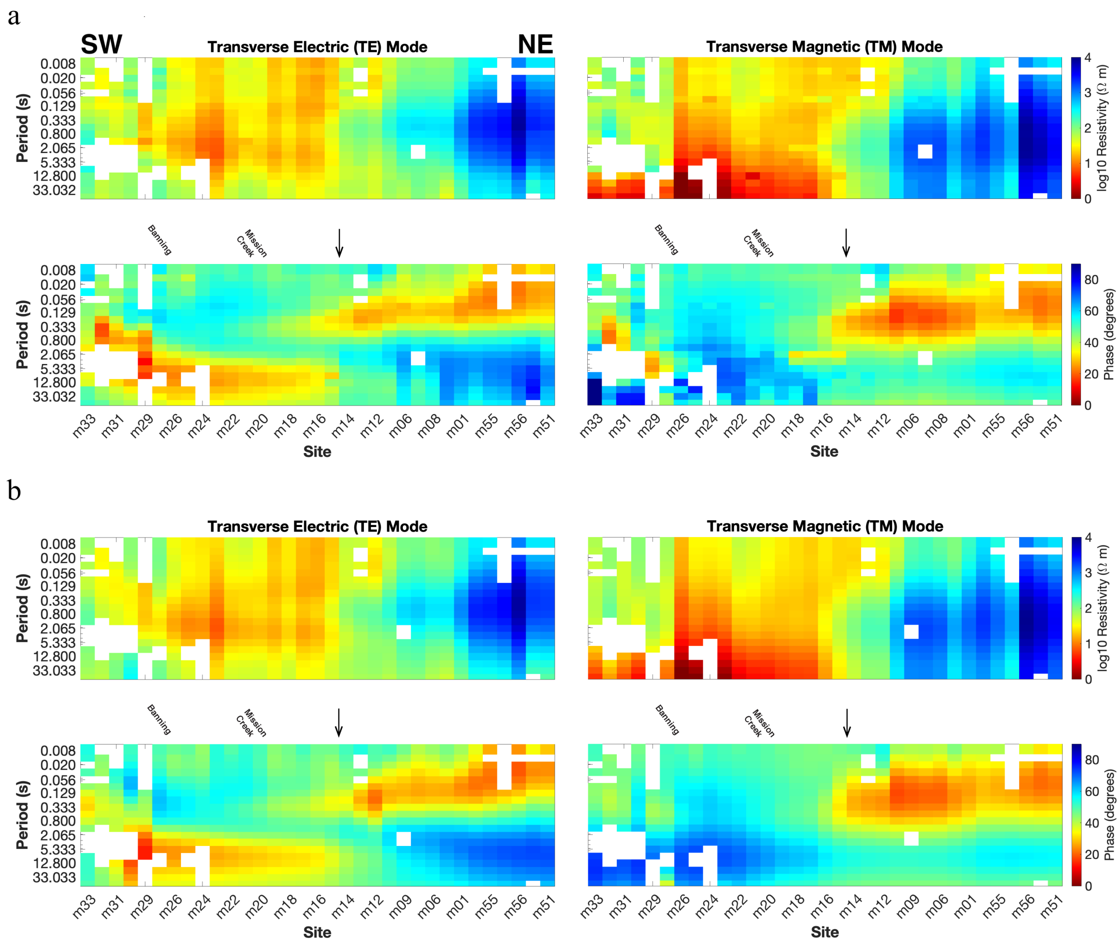

Figure 3: Pseudosections for the TE (left) and TM (right) modes up to 50 s period associated with recorded (a) and modeled (b) data responses. The modeled data correspond to the inverted model in Fig. 4. Differences between (a) and (b) are also illustrated in Fig. S3.

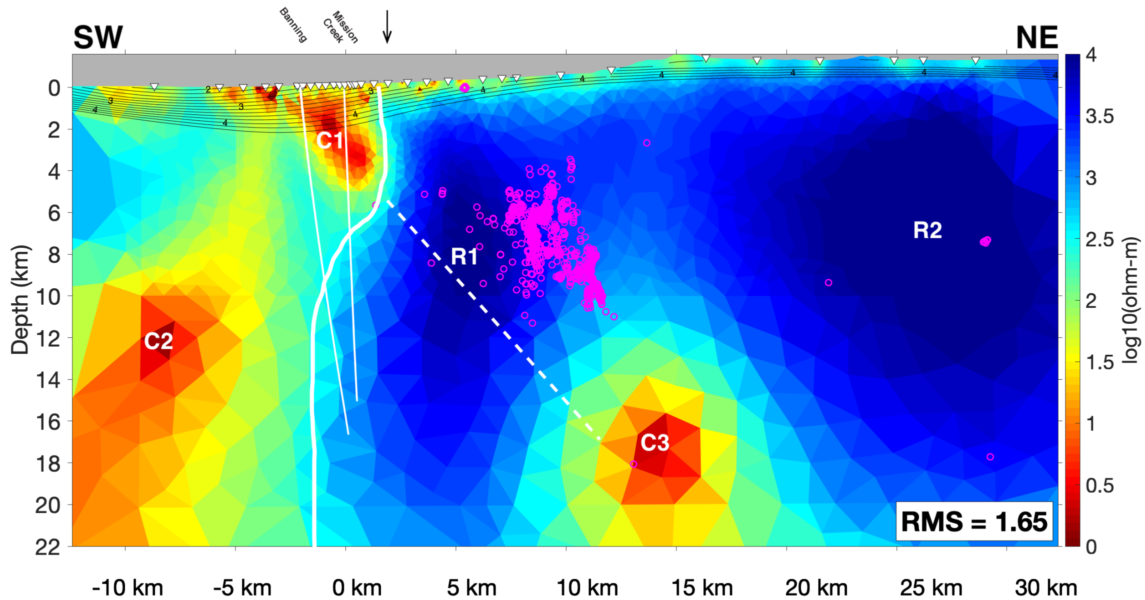

Figure 4: Final 2D inverted model with prominent conductors (C1-C3) and resistors (R1-R2) marked. Magenta circles are local earthquakes within 3 km of this 2D plane. The thick white line highlights a region of sharp resistivity change throughout the crust and represents one (and the preferred) interpretation for the location of the northeastern edge of the shallow SSAF zone and its near vertical geometry at greater depth. The nearby thinner white lines depict geometries of the Banning and Mission Creek strands from the SCEC-CFM5.2 (Fig. 1a). The dashed white line connecting C1 and C3 is an alternate interpretation of SSAF zone geometry at greater depth. Black contours are from the P-wave velocity model of Ajala et al. (2019) from 2 km/s to 4.4 km/s sampled at increments of 0.2 km/s and highlights mostly basin geometry in the central Coachella Valley.

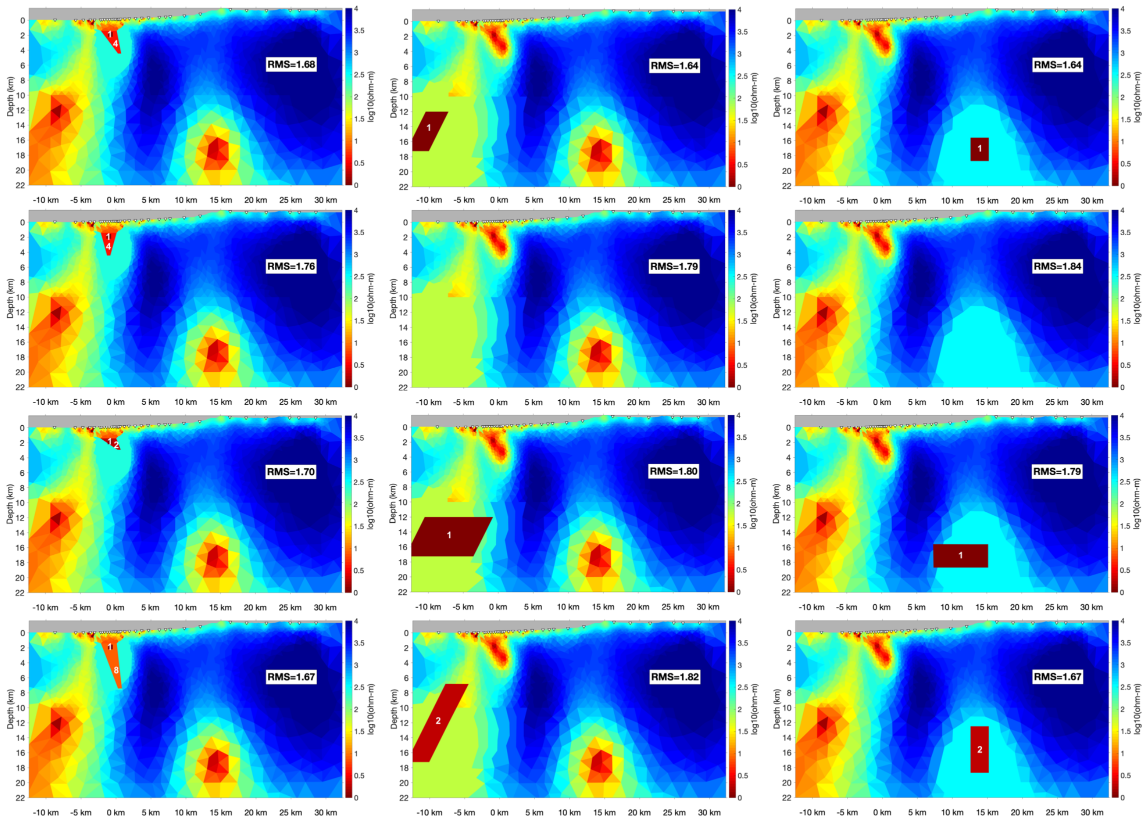

Figure 5: Equivalent resistivity anomaly representations of conductors C1 (left column), C2 (middle column) and C3 (right column) with similar misfits as in Fig. 4 (top row). Lower panels show removals, extensions and translations of these anomalies (all subsequent rows), and, the misfits associated with those alterations. Numbers inside anomalies represent resistivities in Ω.m.

Supplemental Figures

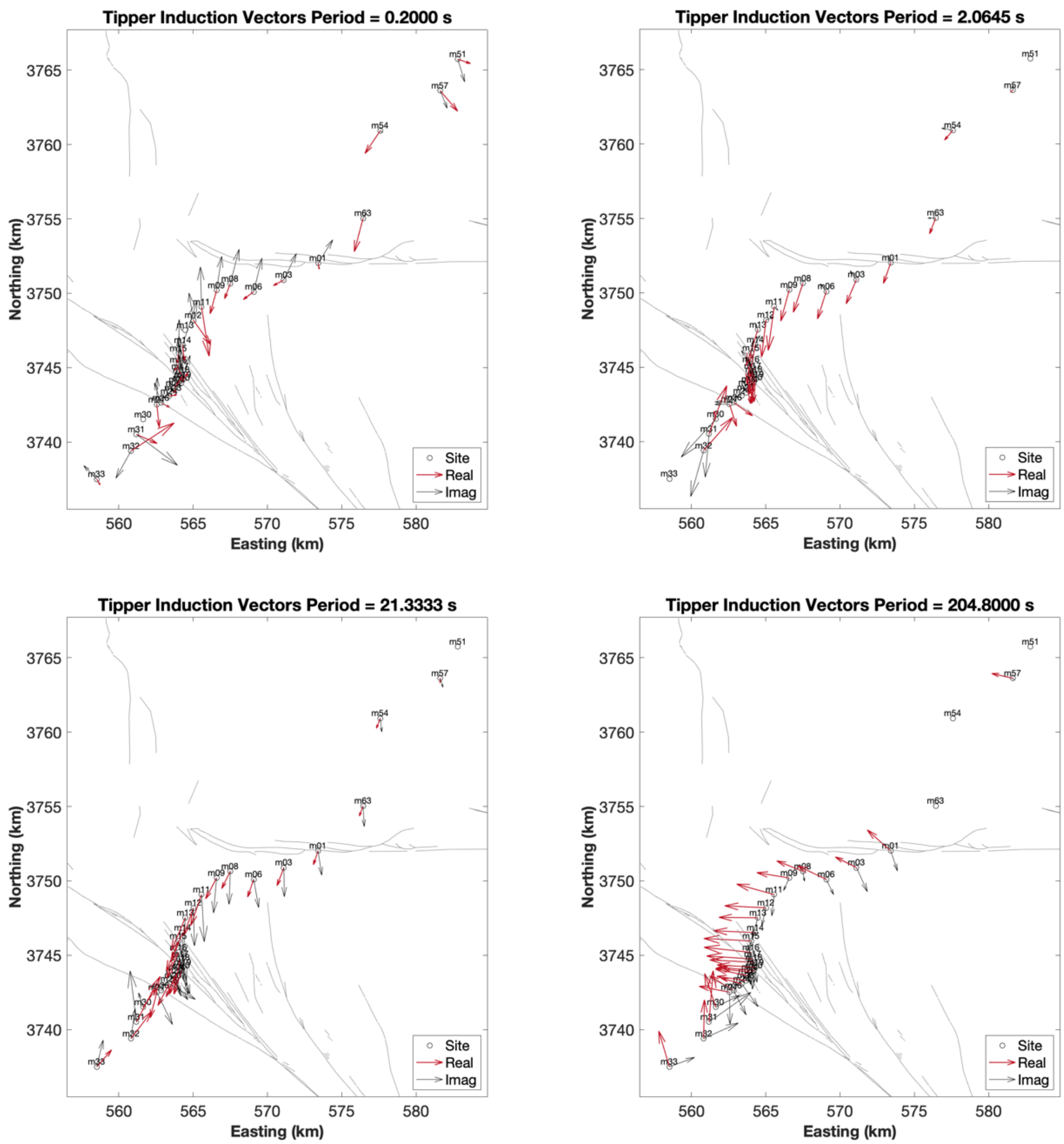

Figure S1: Tipper induction arrows (real-maroon, imaginary-black) from Fig. 2a at periods of approximately 0.2 s, 2 s, 20 s and 200 s plotted in map view. Note the rotation of real tippers away from the SSAF zone and towards a deep large-scale conductor in the northwest at longest periods.

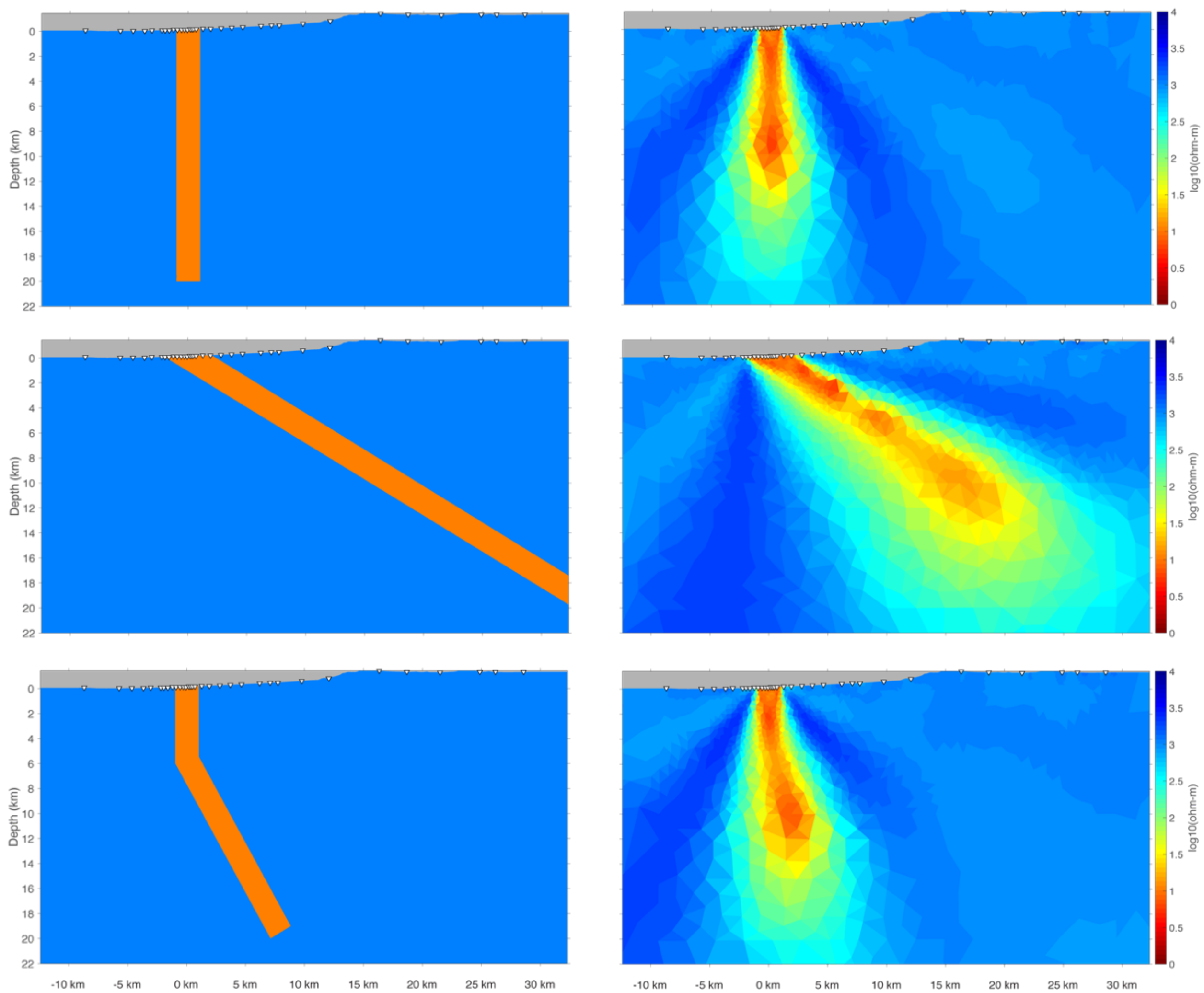

Figure S2: Synthetic forward models (left) and recovered inverse solutions (right) using different fault zone geometries. The geometries are (top) a vertical fault zone anomaly extending from the Mission Creek fault strand surface location to 20 km depth embedded in a surrounding host rock with resistivity of 1000 Ω.m, (middle) same as (top) but for a fault zone with a shallow dip of 30° to the northeast, and (bottom) similar resistivities again but a more geometrically complex fault zone that is vertical down to 6 km depth and starts to steeply dip to the northeast by 60° below that (see main text for details). The synthetic fault zone has a width of 2 km, a resistivity of 10 Ω.m and is embedded in a 1000 Ω.m host rock. The starting half-space for the inverse model has a resistivity of 100 Ω.m. The horizontal to vertical smoothing ratios used during inversion were 0.4 (top), 1.1 (middle) and 0.5 (bottom). All inverse models have a final rms of 1.

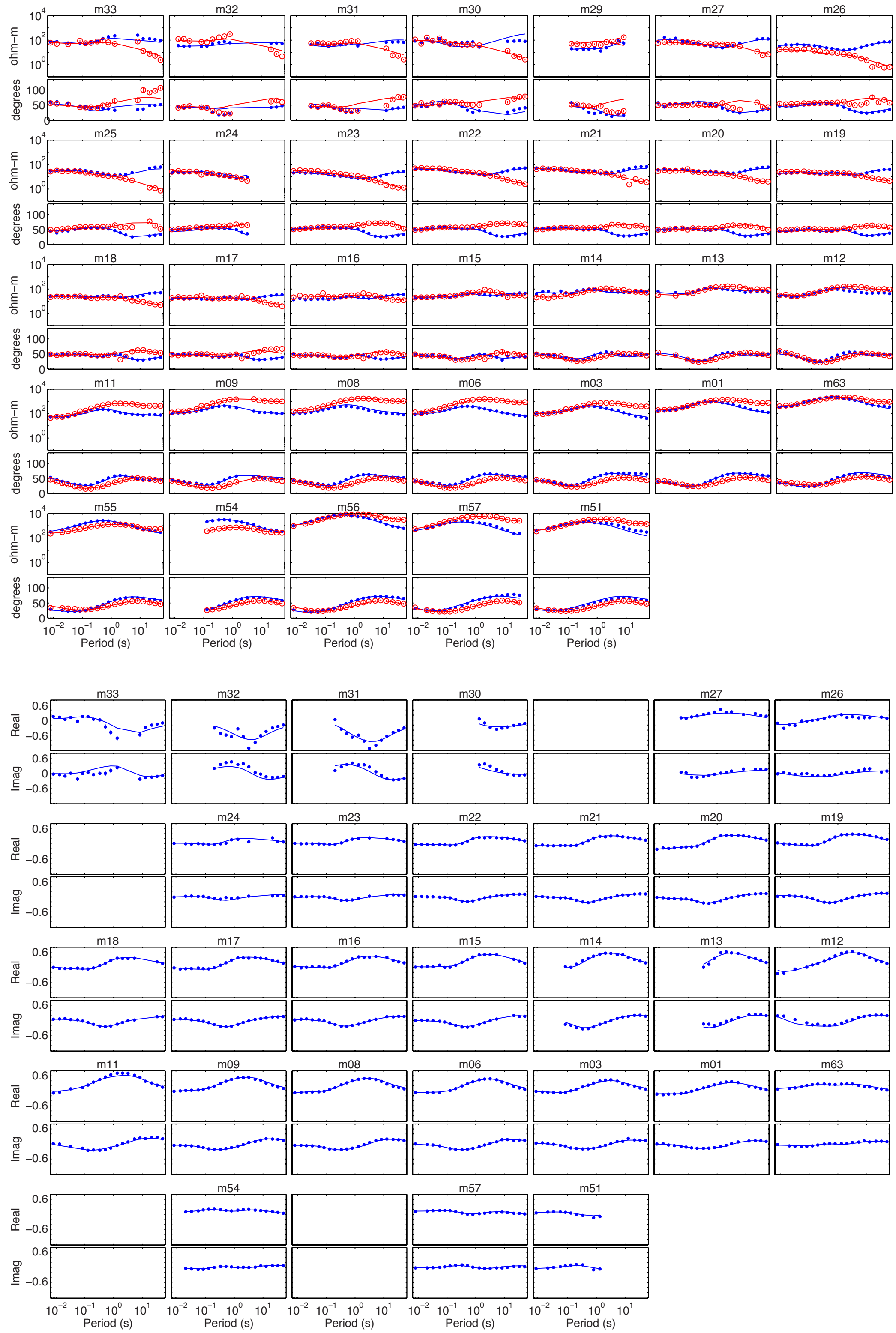

Figure S3: Data (dots and circles) and responses (lines) from our final 2D model (Fig. 4) for TE (top, blue), TM (top, red) and T_{ZY} (across-fault) tippers (bottom, blue).

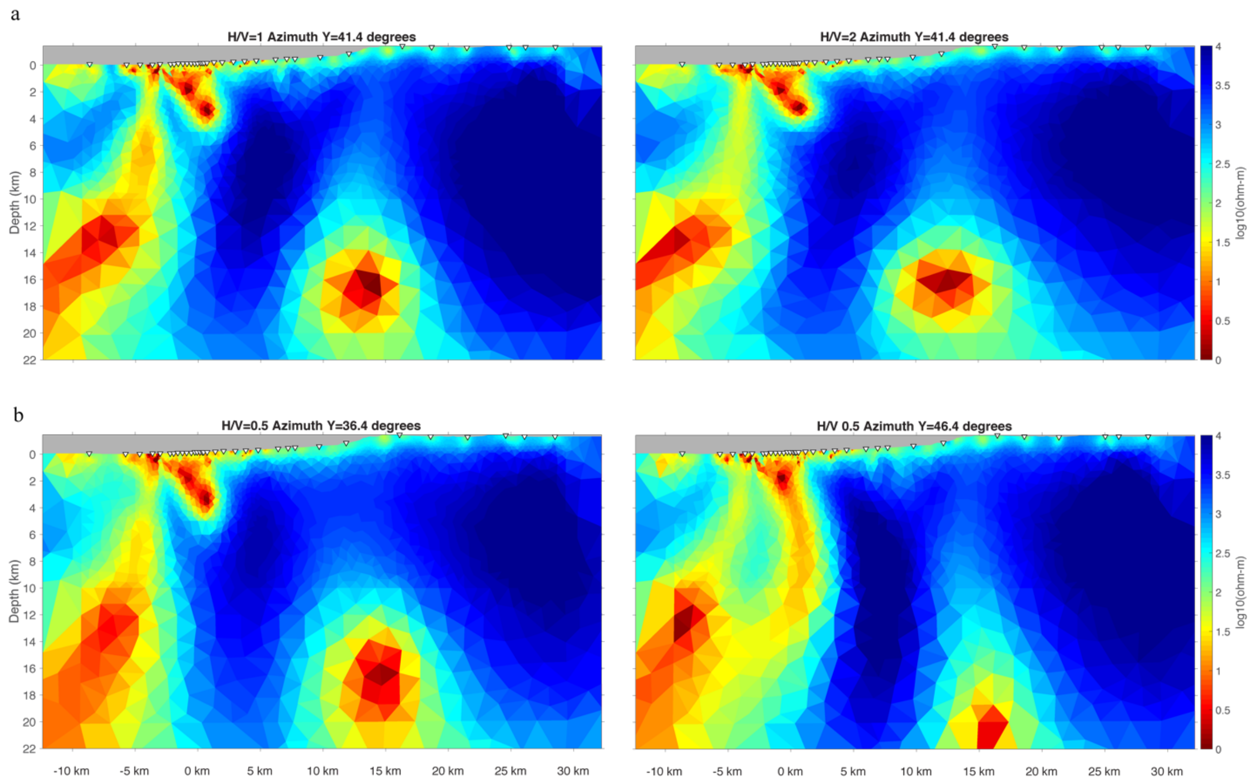

Figure S4: (a) Inversion results using the same data as in Fig. 4, but for a horizontal to vertical smoothing ratio of 1 (left) and 2 (right). (b) Inversion results using the data in Fig. 4 but rotated to X=306.4° and Y=36.4°, and, X=316.4° and Y=46.4° (right), respectively. All other parameters are the same as in Fig. 4. All models have a final rms of 1.65.

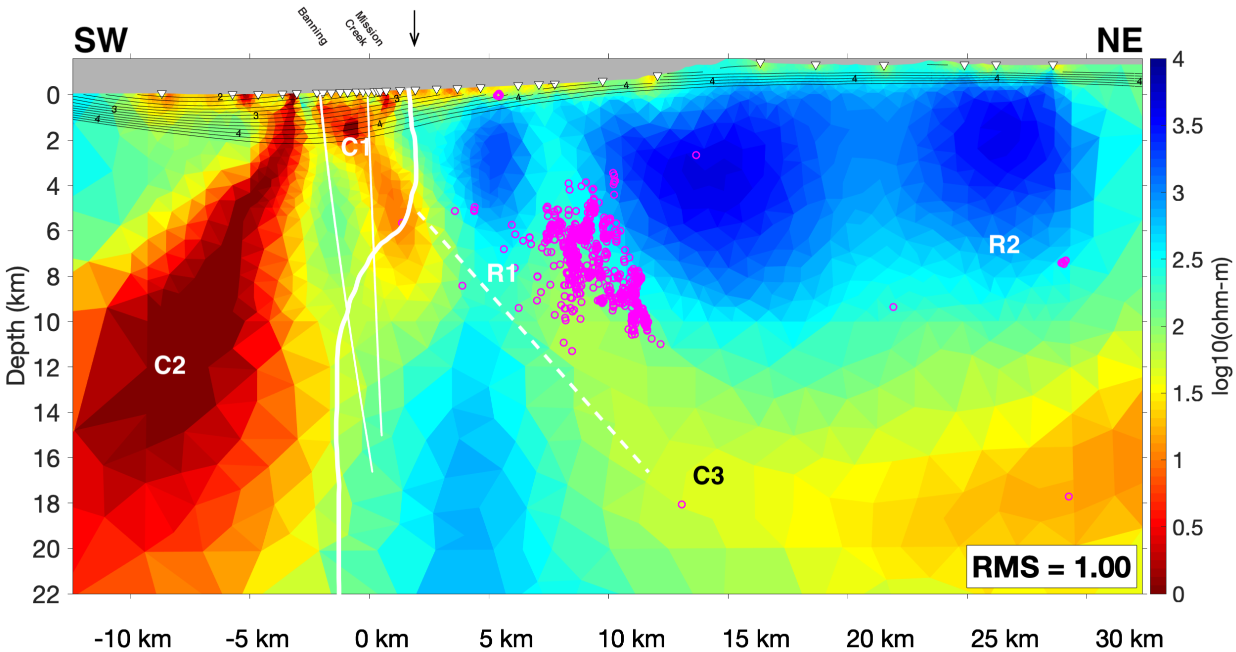

Figure S5: 2D determinant inversion result using all available data (>50 s also). The determinant data are obtained by multiplying the TE and TM mode data after rotation to strike (in-line direction). By definition, tipper data are not included in the determinant inversion. This image represents the smoothest model at a target misfit of rms=1. All references and symbols are in the same locations as in Fig. 4.

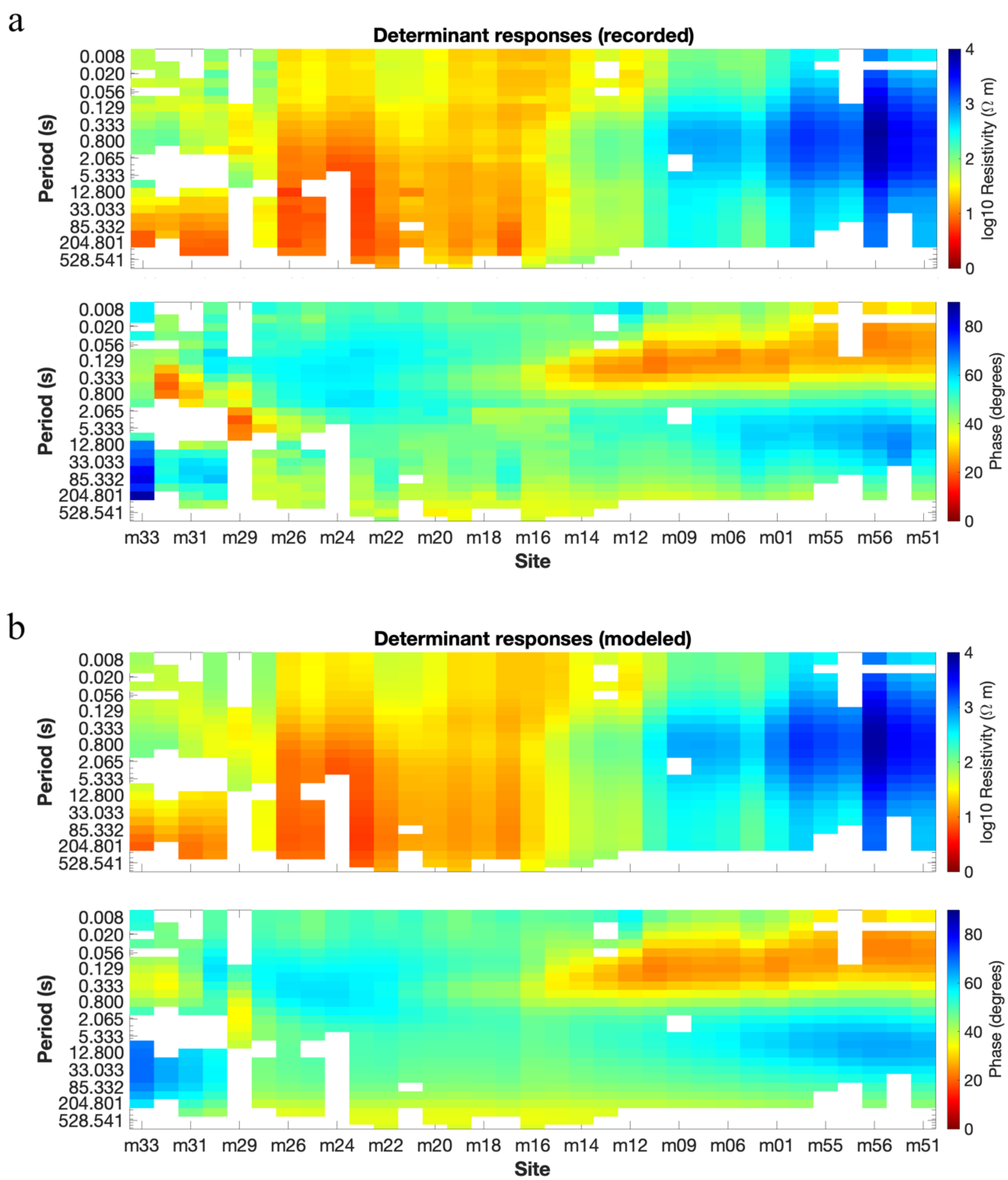

Figure S6: Pseudosections of the determinant data (all periods) associated with recorded (a) and modeled (b) responses. The modeled data correspond to the inverted model in Fig. S5.

Dear editors and reviewers,

We thank you for reviewing and considering the manuscript (GJI-S-21-1108) entitled **"Structural properties of the Southern San Andreas fault zone in northern Coachella Valley from magnetotelluric imaging"** for publication in GJI. The manuscript was recommended for publication after *moderate* revision. The main concern for Reviewer #1 was the influence of 3D structures and data (especially in the southwest) on our 2D modeling approach and interpretations. Reviewer #2 was overall pleased with the state of the manuscript and recommended it for publication as it is. In terms of the concerns about 3D effects, we emphasize that given the overall 2D nature of our selected data (and the mostly 2D shallow crustal transform plate boundary they represent), the quasi-linear station layout and the local irregular topography, a 2D MARE2DEM inversion approach is best (but not perfect) and the resultant 2D model accurately represents the underlying structure at the depths presented. To corroborate this, we added determinant data inversion results to the manuscript (Section 4 & Figs S5-S6). These type data were recently embedded in the MARE2DEM inversion package, so have all the advantages stated above and in addition are less susceptible to the distorting effects of 3D structures in cases where the region and data are mostly 2D (i.e., our study region). The resultant determinant inversions were indeed consistent and comparable to our original 2D inversion (Figs 4 & S5), emphasizing that the 3D parts of the limited dataset employed and depths under investigation are minor and are not significantly distorting our preferred 2D model (Fig. 4) and interpretations (Section 5). Finally, and in response to the minor comments from both reviewers, we also modified several of the figures and the text in order to improve accuracy, clarity and presentation.

Below we provide detailed replies to the comments of the editors and the two reviewers (noting that line numbers have now changed in the revised version). We also upload an annotated version of the revised manuscript ("Share_etal_2022_trackchanges.pdf") showing all the changes made to the original submission.

We thank you all again.

Yours sincerely,

Pieter-Ewald Share for all authors

Editor's Comments to the Author:

Dear authors,

Thank you for submitting your manuscript GJI-S-21-1108 to Geophysical Journal International for which we have received two reviews.

Both experts come to a quite different assessment although both of them find the topic of your manuscript interesting and publishable. Reviewer #2 has only some minor comments and in summary finds your manuscript "publishable as it stands". Reviewer #1 has some major issues and asks for major modifications. He/She is not convinced that the data set is consistent with a

2D interpretation along the entire profile and for the entire frequency range. Looking at the phase tensors together with the directions of the inducting vectors suggests that a 2D approach might be too much of a simplification. He/She suggests two possible ways to solve this issue; either with 2D modelling studies or by measures of synthetic 3D studies to evaluate possible artefacts. As a comment from my side, it might be worthwhile to have a look at Cruces-Zabala, J., Ritter, O., Weckmann, U., Tietze, K., & Schmitz, M. (2020). Magnetotelluric imaging of the Mérida Andes and surrounding areas in Venezuela. Geophysical Journal International, 222(3), 1570-1589 or Cruces-Zabala, J., Ritter, O., Weckmann, U., Tietze, K., Meqbel, N., Audemard, F., & Schmitz, M. (2022). Three-dimensional magnetotelluric imaging of the Mérida Andes, Venezuela. Journal of South American Earth Sciences, 103711.
Another issue concerns the resolution test presented in Figure 5. As indicated by reviewer #2, an original model that apparently achieved the best fit to the data will in most cases have a higher rms if additional features are included. Allowing the subsequent inversion to either keep or omit features in the starting or prior model, will probably lead to a less biased result.
As additional modelling studies are necessary, I have classified the changes required as "moderate revision". I expect to see the majority of the reviewers' comments implemented in your revision. A point-by-point response will be needed to allow me to see how you have implemented the requested changes. For easier recognition please mark changes in the revised manuscript e.g. by using different colour.

Kind regards,
Ute

We thank you for all the substantial input and suggestions and for the literature to review. We have taken all these on board while revising the paper. After weighing the options, we concluded it was most appropriate to supplement the original manuscript with results from MT determinant inversions. These are embedded in MARE2DEM, so have all the advantages of that package and thus allows a more "apples-to-apples" comparison with our preferred model (Fig. 4). The determinant inversion also provides a less distorted (but smoother) 2D slice through a region that is predominantly 2D but contains some 3D features (e.g., our study region). In the end, all the determinant inversions (Fig. S5-S6 shows one example) were highly consistent with our preferred model, demonstrating that the Fig. 4 result is not significantly affected by the minor amounts of 3D data present and that our model interpretations are reliable.

Please note, because of the additional work required for the determinant inversions, we have added another co-author to the manuscript, i.e., Dr. S. Wang, who steered and performed these inversions and helped with the interpretation of results.

Please see below for detailed responses to Reviewer #1 on the issue of the resolution tests in Fig. 5 as well as detailed responses to all the other comments from both reviewers.

We hope the resubmitted version is satisfactory for eventual publication in GJI. Thank you again.

Assistant Editor's Comments to the Authors:

As you are not paying for colour printing, you should ensure that all of your figures can be understood when printed in black & white, by e.g. changing line styles and plotting symbols, adding suitable labels etc., and avoid distinguishing features by colour alone in captions and legends.

Please ensure that all textual labels in figures are at least as large as the caption text; any smaller and they become too difficult to read.

We would like to change our selection, and request that the figures in print be in color also. We will pay the necessary additional fees. Please update the submission accordingly.

Reviewer: 1 - Anonymous

Comments to the Author(s)
The manuscript showcases a magnetotelluric study across the southern San Andreas Fault (SSAF) which is modelled and interpreted based on a 2-D modelling approach. The authors argue that for the relevant period range, the 2-D assumption is sufficiently fulfilled. Based on the resistivity model, they infer a near-vertical fault plane between 2 and 20 km depth, but cannot exclude a fault dipping to the NE. The two scenarios are discussed in view of existing additional information from geology and seismology.

MT is generally able to infer geometries and other properties of fault zones. The work is interesting and relevant since it studies a section of the SAF which is poorly understood so far, but poses a significant earthquake risk. Overall, the manuscript is well written and structured and the figures are usually illustrative. In principle, I consider the work suitable for publication in GJI, after revision.

Thank you for your thorough review. Please see below for detailed responses.

I have one major comment: I am not convinced that the 2D model and interpretation of the data set provides a reliable image for the first 15 km at the SW profile end. Yet, it is this section which is crucial for the delineation of the SAF.

The authors argue that 2D conditions are fulfilled for the data set for periods up to 50 s and, thus, 2D modelling and interpretation are sufficient. I agree that 2D properties are fulfilled up to 50 s for the NE half of the profile (NE of site m14) based on the phase tensor properties displayed in Fig. 2. But, for sites to the SW of site m14, 2D conditions are fulfilled for much shorter periods only. For sites m28- m16, the 2D assumption seems reasonable up to periods of 10 s, for periods of 12.8 s and above data are definitely 3D. For the three leftmost sites m33-m31, I would even interpret data > 1 s as 3D; m30 and m29 appear 3D throughout the available period range.

Also, real and imaginary parts of induction arrows at 20 s (Fig. S1) show significant deviations from being (anti)parallel nearly everywhere, in particular for sites m33 to m11, and point at a 3D subsurface.

Thanks for these key observations. Prior to describing our remedy for the 2D versus 3D issue below, a few responses are warranted. First, we agree with the above points overall. It is clear that some of the data have 3D characteristics. We note this in the text and re-emphasize it in the revised version (L. 180-188 & 273-275). However, it is also clear from our analyses and your description above that the vast majority of data up to 50 s are 1D to 2D in nature and thus lends itself more to a 2D modeling approach. Second, the sites to the southwest are noisiest (L. 143-149). Thus, the interpretation of 3D structure to the extent mentioned above for those sites hinges on the fact that we know the contribution to those anomalous impedances (Fig. 2) from the noise alone, which we do not. The rapid and non-smooth changes in phase tensor characteristics for neighboring periods at sites m29-33 suggest that noise is indeed playing a significant role at those sites. During inversion, increased error bars for these sites (L. 212-213) helps compensate for this noise and any minor 3D structures that may be present.

I see two potential ways to approach this issue:

1) Performing a sincere and thorough analysis and discussion of the limitations of modelling, resolution, and interpretation of the 2D-only approach. This would require more 2D modelling. For example, what happens if all 3D data are omitted? How much structure can then be revealed? Is there still enough resolution to discriminate between the various scenarios?

2) Performing additional 3D modelling of the data set. The current version of the manuscript mentions that such tests were performed and "features of the 3D model were consistent with our 2D inversions, but lacked the resolution of the Mare2DEM finite element code". Are they consistent particularly in the 3D (SW) section of the survey? Do these 3D models even shed light on the geometry of the SAF? Based on the comments to the initial version of the ms and related answers of the authors I conclude that the 3D models appeared homogeneous at lower crustal depths and did not allow to make inferences on the fault geometry.

Thank you for these suggested solutions. It has helped greatly improve the manuscript. After weighing the options, we decided to go with option (1). A 3D approach has its own drawbacks (e.g, can't constrain off-profile extent of anomalies, lacks the resolution of a finite-element code) and we have concluded that the majority of data at <50 s is 1D/2D, the underlying transform plate boundary structure is expected to be approximately 2D, and that the advantages of a finite-element algorithm lend itself well to our specific high-relief setting and quasi-linear MT array.

As a supplementary to the existing results, we executed several MT determinant inversions. These inversions provide a less distorted (but smoother) 2D slice through a region that is predominantly 2D but contains some 3D features (e.g., our study site). Also, it is already embedded in the MARE2DEM package so has the advantages of that finite-element algorithm and allows a more "apples-to-apples" comparison to the results presented in this manuscript, including our preferred model (Fig. 4). Results from all the determinant inversions we ran were highly consistent with Fig. 4, especially in the conductive southwestern end of study region. This demonstrates that the Fig. 4 result is not significantly distorted by the minor amounts of 3D data and that our model interpretations are reliable. This holds true even in the case where we add all available data (>50 s) representing a much more expanded 3D dataset. Example determinant inversion results were added as new Figures S5 and S6. We added these in the Supplementary as we want to focus the reader on our preferred model, Fig. 4, which is constrained by a larger and more diverse dataset (TE, TM & tipper) and is less smooth and thus highlights better the rapid changes in fault zone structures that are the key geologic targets in this study. The following description of these results has been added as L. 271-290 in the main manuscript.

"The model in Fig. 4 is our preferred result as it is equally well constrained by TE, TM and tipper data (Fig. S3) and the majority of that data at periods <50 s is 2D in nature with a consistent near fault-parallel strike (Fig. 2). However, as noted in Section 3, even at <50 s some stations and periods exhibit 3D characteristics, e.g., at the southwestern and northeastern sites (Fig. 2). As a supplement and to test the effects of these minor 3D features in a predominantly 2D upper to mid crustal region, we additionally applied a 2D determinant inversion (Pedersen & Engels 2005; Wang et al. 2020; 2021). This type of inversion has been shown to produce less-distorted 2D model representations of a predominantly 2D region that also includes 3D structures (Wang et al. 2020). However, this lower distortion comes at the cost of larger model smoothness. The algorithm employed is embedded in the MARE2DEM package, which facilitates comparison with Fig. 4. During inversion, we used the same impedance tensor data (not tippers), matching errors, and the model and inversion settings described above. Overall, all our resultant determinant inversion models were consistent with Fig. 4. In fact, even when we included data from all available periods, which constituted a significant increase in 3D data, the determinant inversion result was still comparable to Fig. 4 (Fig. S5-S6). In Fig. S5, anomalies C1-3 and R1-2 are all present, albeit the fact that C2 is more conductive and extends to shallower depths, and the region containing R1, R2 and C3 is generally smoother with R1-2 lower in resistivity and C3 smeared towards the northeast where there is less station coverage and the data at longest periods reflect 3D structure (Figs 2 & S1)."

I am agreeing with and supporting the first comment of Reviewer #1 to the initial version of the manuscript and would like to cite this persons words here again, because it has already been said, but I do not find this point addressed sincerely in the revised version:

"Should we believe the 2D image or the 3D image? While 3D inversion has the benefit to account for 3D effects in the data, it is known that regularization in ModEM often emphasizes the shallow parts of the model. What is more, weakly constrained offprofile structures may account for some aspects in the data as well. Therefore, 3D inversion of profile data is not necessarily superior to 2D inversion, and both 2D inversion and 3D inversion of profile data must be evaluated with equal care. The discussion of the 3D model must be broadened to make it of value - or omitted completely, if arguments are presented to use a 2D interpretation only. In any case, more work is required here."

We hope this issue has been adequately addressed above.

Besides, I am not really sure what I can learn from the resolution study in Fig. 5. I can only guess from the very short description of this analysis in the main text (please expand!) that the test is using pure forward simulations, where structures of the final inversion model are modified and the response of this modified model is compared to the response of the original model and the measured data. The significance of such comparisons, though, is limited. The inversion result represents a (local) minimum in the misfit space. Any, even through "small", modification of this usually leads to an increase of the data misfit. For a more meaningful test, such alternative subsurface structures would have to be included in the starting model and inversion has to be rerun subsequently. Only such a test would enable the inversion scheme to (a) find a suitable model around this assumption or to (b) fail to fit the data adequately, and would allow to accept or reject the underlying hypothesis. What about other apparent hypotheses: A potential connection between C1 and C2? Two conductive fault strands?

Thanks. It is true that once a minimum misfit is reached then small changes in conductive parts of the model space can lead to large changes in misfit. However, this holds most true where your data sensitivity to model parameters is relatively high, otherwise it does not. MT data are not as sensitive to resistors and, also, to conductors located deeper than the skin depth of the employed frequencies. The purpose of Figure 5 is to highlight to the reader critical parts of the Fig. 4 model (C1-C3) that potentially lie in this type of nullspace. For example, near surface areas with less station coverage and the bases of conductors are more poorly resolved. This is the reason a connection between the base of C1 and the top of C2 was not more explored as that is intrinsically a poorly resolved region (e.g., Fig. S4 shows a connection while other models do not). Also, in general, changes at shallow depths have greater effects on misfit compared to changes at depth. The former shows higher data sensitivity to model parameters compared to the latter. These points are now more clearly stated in L. 254-270:

"Given that some regions in the model space are more poorly resolved than others, such as near surface areas with less station coverage, greater depths in general, and regions beneath conductors (e.g., Chave & Jones 2012), we applied a few conductance-preserving (conductivity-thickness product) alterations of particularly C1-C3 to test if small changes in their properties are allowed without significantly affecting the misfit (i.e., changes within the nullspace, Munoz & Rath 2006). MT data are most sensitive to changes in conductance rather than conductivity, so by preserving conductance these tests highlight how changes in the geometries and locations of C1-C3 affect data misfit. They also provide an indication of their relative influence on misfit and, therefore, the relative data sensitivity to these conductive parts of the model space. In general, the tests show that only small changes in C1-C3 are allowed without significantly increasing the model misfit (Fig. 5). Specifically, the steep northeast dipping geometry of anomaly C1 is well resolved as a more vertically orientated structure in the inverted model increases the rms to ~1.8 (Fig. 5). And, the resistive region separating C2 and C3 is similarly well resolved as extensions of either C2 or C3 towards the other lead to large increases in rms (Fig. 5). For example, extending C2 only 6 km to the northeast produces the same significant increase in rms as removing it from the inverted model altogether (Fig. 5)."

Based on the above considerations I recommend publication of the manuscript after major revision.

Thank you again. We hope the revised version is more suitable for publication in GJI.

Additional comments:
L 118-120: How long did the logger record? 8 hours + 10 minutes or 20 hours? L 121: Please provide the distance to the remote site in km.

We have added "The ZEN was programmed to record in a sequence that started with 256 Hz sampling for 8 hours followed by a burst of 4096 Hz sampling for 10 minutes. This sequence repeated several times within the ~1-day recording window." in L. 117-119 to clarify the statement about recording. The distance (i.e., ~66 km) to remote reference has also been added to L. 121.

L 128: While I agree, that frequencies > 500 Hz are probably not relevant to the study of the SAF, I do not really understand why neighbouring sites should be too far away for remote reference processing of frequencies > 500 Hz. Please explain.

Agreed, greater clarity is required here. We have modified the sentence L. 127-130 to read "Without a remote reference and with coherent high-frequency noise present across neighboring sites (spaced <500 m near the SSAF), the single-station responses at these very high frequencies may have only yielded biased estimates of near-surface resistivities."

Fig. 1: Magenta circles and black dots are very hard to see both printed in original size but also when zooming in into the pdf. Add north arrow to b) to make it easier to understand the orientation of the coordinate system.

Thanks. We enlarged the size of the black circles to clarify and have removed the magenta circles from Fig. 1. The latter omission reduces clutter and these events are already highlighted in Fig. 4 and in the new Fig. S5. The north arrow has been added to (b).

Fig. 2: Consider adding labels SW and NE to the profile to facilitate grasping of the figure. Fig. 3: Labels are extremely small and hard to read, increase font size.
Fig, 4: As in Fig. 3, labels are extremely small. Thin white lines hard to see when printed.

Noted. We have made all these requested figure changes.

Reviewer: 2 - Anonymous

Comments to the Author(s)

Thanks for the revision! A very clear manuscript, well and concisely written, with all the required information provided.

Thank you for reviewing and considering this suitable for publication after minor edits.

In the abstract, line 32, it is stated that ... (1 Ohm-m at 2 km and 12 km ...). It is unclear, to what distance or depth the value of 2 km refers. It cannot be depth because the sentence refers to teh ductile crust, but is also does not seem to refer to distance. Just an error?

Thanks. The 1 Ohm-m at 2 km refers to the observed maximum within anomaly C1, the one at 12 km depth the maximum in C2. This has been clarified in the abstract by splitting up the two descriptions into two different parentheses.

line 50: ..., damage zone, ... insert (zone)

The word "zone" is redundant here because we start that part of the sentence with a category, i.e., fault *zone*, and then list the properties in that category that we are trying to inform. Though, we did swop the words "zone" and "geometry" to improve readability.

line 78: inducing magnetic fields ... this is a bit oversimplified, because the magnetic field has also secondary components, to be precise ...

Correct. The "inducing" reference has been removed.

line 202: 10^5 Ohms for the air maybe a bit too low

This is the representative value used in other successful MARE2DEM studies so we keep it as is.

line 328: ... evolves ... it should be plural here (evolve)

Corrected.

Figure 4: The thin white lines are difficult to discern. Perhaps use thicker (dashed) lines

We made the lines thicker.

Structural properties of the Southern San Andreas fault zone in northern Coachella Valley from magnetotelluric imaging

Pieter-Ewald Share[1*], Jared R. Peacock[2], Steven Constable[1], Frank L. Vernon[1] and Shunguo Wang[3]

Deleted: and

[1]Institute of Geophysics and Planetary Physics, University of California San Diego, La Jolla, CA

[2]Geology, Minerals, Energy, and Geophysics Science Center, USGS, Moffett Field, CA

[3]Department of Electronic Systems, Norwegian University of Science and Technology, Trondheim, Norway

[*]Now at College or Earth, Ocean, and Atmospheric Sciences, Oregon State University, Corvallis, OR

Corresponding author: Pieter-Ewald Share (pieter.share@oregonstate.edu)

Geophysical Journal International 2022, in review

Deleted: ¶

Deleted: ¶
¶
¶

Key words: Continental tectonics: strike-slip and transform; Fractures, faults and high strain deformation zones; Electrical properties; Magnetotellurics

Summary

The Southern San Andreas fault (SSAF) poses one of the largest seismic risks in California. Yet, there is much ambiguity regarding its deeper structural properties around Coachella Valley, in large part due to the relative paucity of everyday seismicity. Here, we image a multi-stranded section of the SSAF using a non-seismic method, namely magnetotelluric soundings (MT), to help inform depth-dependent fault zone geometry, fluid content, and porosity. The acquired MT data and resultant inversion models highlight a conductive column encompassing the SSAF zone that includes a 2-3 km wide vertical to steeply northeast dipping conductor down to ~4 km depth (maximum of ~1 Ω.m at 2 km depth) and another prominent conductor in the ductile crust (~1 Ω.m at 12 km depth and slightly southwest of the surface SSAF). We estimate porosities of 18-44% for the conductive uppermost 500 m, 10-15% porosity at 2 km depth and that small amounts (0.1-3%) of highly interconnected saline fluids produce the deeper conductor. Located northeast of this conductive region is mostly resistive crust indicating dry crystalline rock that extends down to ~20 km in places. Most of the local seismicity is associated with this resistive region. Located farther northeast still is a conductive region at >13 km depth and separate from the one in the southwest. The imaged anomalies permit two interpretations. The SSAF zone is vertical to steeply northeast dipping in the upper crust and (1) is near vertical at greater depth creating mostly an impermeable barrier for northeast fluid migration or (2) continues to dip northeast but is relatively dry and resistive up to ~13 km depth where it manifests as a secondary deep ductile crustal conductor. We prefer interpretation (1), but more MT investigations are required.

Deleted: 2 km and

Deleted: beneath

Deleted: a large resistor (maximum of ~10,000 Ω.m)

Deleted: vertically

Deleted: and hosts most

Deleted: .

Deleted: separate

Formatted: Font: Not Italic

1. Introduction

Deleted: ¶

The Southern San Andreas Fault (SSAF) has not produced a M>7.5 event for >300 years and is estimated to pose one of the largest seismic risks in California (Weldon et al. 2005; Sieh & Williams 1990). Several properties of the SSAF such as fault zone damage, geometry, and fluid content remain poorly understood despite several geoscientific studies (e.g., Catchings et al. 2009; Lindsey & Fialko 2013; Ajala et al. 2019). Informing these properties is essential as they may play key roles in the magnitude and subsequent shaking from future large events (e.g., Roten et al. 2015; Biasi & Wesnousky 2016).

Deleted: , damage

One outstanding question is whether the SSAF at depth, if well localized as expected for a mature plate margin (Montési 2013), is near vertical or dipping to the northeast. In the Southern California Earthquake Center Community Fault Model (SCEC-CFM5.2, Nicholson et al. 2017) it is mapped as a vertical fault in the Coachella Valley (Fig. 1a). In contrast, analyses of interseismic strain fields (Fialko 2006; Tymofyeyeva et al. 2019) and potential field data (Fuis et al. 2012; 2017; Langenheim & Fuis 2021) point to a northeast dipping SSAF similar to its neighboring strand in San Gorgonio Pass (Fig. 1a), the latter being well constrained by small to moderate sized events (Jones et al. 1986; Nicholson 1996). A deep northeast dipping SSAF is supported by more abundant seismicity on that side of the surface SSAF, and a large structure with a prominent seismic velocity contrast (bimaterial interface) intersecting this seismicity (Fig. 1a, Share & Ben-Zion 2016). However, these features can also be attributed to secondary faults in the northeast (Fig. 1a, Nicholson et al. 2017). Much of our inability to resolve this fundamental question about deeper SSAF structure is owed to the general lack of seismicity in the region (Ross et al. 2019), which is essential to delineate fault geometry (e.g., Magistrale & Sanders 1996;

Deleted: Montesi

Carena et al. 2004) or in high-resolution seismic imaging studies (e.g., Share et al. 2019). Thus, more studies using non-seismic geophysical tools are needed to help inform SSAF properties and its associated seismic risk.

Here, we use an established electromagnetic imaging method, namely magnetotelluric soundings (MT, Cagnaird 1953), that does not depend on seismicity (or paucity thereof as in the study region) as a source, to image for the first time the electrical resistivity structure of the SSAF throughout the crust. MT is a passive geophysical tool that measures ubiquitous natural variations in the Earth's magnetic field and induced electric fields generated in the subsurface. Resistivity within the Earth is then derived from frequency-dependent transfer functions (MT tensor) between magnetic and electric fields.

Deleted: inducing

Deleted: fields

Deleted: induced

Deleted:

MT data are preferentially sensitive to high conductivity (inverse of resistivity) regions within the Earth (Chave & Jones (2012) and references therein). Relative to the deeper mantle continental crust is electrically resistive (Schwarz 1990) except for anomalous regions where conductive materials (e.g., aqueous fluids, graphite, melts) form interconnected networks (e.g., Bahr 1997). Thus, active crustal fault zones are optimal targets for MT imaging, where damaged and deformed rocks create pathways for conductive fluids to percolate through the crust, and strain localization forms a mechanism to connect fluids within these weakened zones (Becken & Ritter 2012). Structure, damage, and deformation need not always be symmetric about a fault core and interconnected fluids can be distributed asymmetrically with little fluid migration across an impermeable fault (e.g., Caine et al. 1996; Bedrosian et al. 2004). MT has been successfully used to infer fault zone properties such as amount of damage, fluid content, geometry, and strain conditions in central California (e.g., Becken et al. 2011; Tietze & Ritter 2013), Japan (Ogawa &

Honkura 2004; Yoshimura et al. 2009) and Turkey (Turkoglu et al. 2008). Despite these successes, MT has yet been broadly applied in Southern California.

In this study, we apply MT imaging to a section of the SSAF in northern Coachella Valley near the Thousand Palms Oasis Preserve where the Mission Creek and Banning fault strands merge (Fig. 1b). Despite ongoing debate over which strand is more active in present day, both are well located at the study site using offsets in landforms and lithology and trenching data (e.g., Fumal et al. 2002; Blisniuk et al. 2021). Near the surface, these strands together with other minor faults comprise a ~3 km wide SSAF zone embedded in Pliocene and Pleistocene stratified rock with Coachella Valley Quaternary sediments to the southwest (up to ~2 km thick in central Valley, Ajala et al. 2019), thinner sediments immediately northeast of the Mission Creek strand and the Little San Bernardino Mountains (pre-Cenozoic metamorphic and crystalline rocks) outcropping ~10 km farther northeast (Rymer 2000). The presence of several oases indicates a fault zone acting as a conduit and/or barrier for aqueous fluid flow (Catchings et al. 2009), making it an attractive MT target. We collected data in 2019 along a linear array transecting the SSAF around the Preserve supplemented by stations from a neighboring 2017-2018 array located in the Joshua Tree National Park (Fig. 1a) to image electric resistivities in the area. The abundant seismicity to the northeast is ~10 km from the Preserve and locates at 4-11 km depth (Fig. 1a). Analyzing MT data that span the SSAF zone and a significant area to the northeast allows us to investigate fault zone resistivities and its connection to local seismicity.

2. Data and Methods

The MT imaging was based on ~1-day long recordings of natural variations in Earth's electromagnetic field at 27 sites crossing the SSAF in 2019 and 6 sites located in Joshua Tree in 2018 (Fig. 1a). These sites were acquired using the Zonge International 32-bit ZEN data logger with ANT-4 magnetic induction coils and Borin Ag-AgCl electrodes with 50 m dipoles. The ZEN was programmed to record in a sequence that started with 256 Hz sampling for 8 hours followed by a burst of 4096 Hz sampling for 10 minutes. This sequence repeated several times within the ~1-day recording window. Accompanying the 2019 survey was a magnetic remote reference installed at a low-noise site in the Borrego Desert (33.271608° N 116.064469° W, ~66 km away). This site consisted of a Scripps marine data logger (Constable 2013) to which a GPS clock had been added, collecting data from two EMI-BF4 induction coils oriented north-south and east-west. Magnetic north was used for orientation during all installations. These recorded continuously at 500 Hz for the duration of the weeklong survey. Given the depths and scale of investigation in this study and that >500 Hz data did not exist for the remote reference site, we excluded the 4096 Hz ZEN data from further analysis. Without a remote reference and with coherent high-frequency noise present across neighboring sites (spaced <500 m near the SSAF), the single-station responses at these very high frequencies may have only yielded biased estimates of near-surface resistivities. To better limit very near-surface properties, water samples from the local oases were collected (Fig. 1b) and their resistivities were measured using a laboratory 4-electrode setup. Both samples had similar measured resistivities of 6.2 Ω.m (18.6°C) and 5.9 Ω.m (18.5°C). Finally, for uniformity, all ZEN data were upsampled to 500 Hz and reformatted to conform to the Scripps marine data format.

Deleted: continuously

Deleted: ~

Deleted: at 256 samples per second (sps) with 10-minute

Deleted: sampling at

Deleted: sps in between

Deleted: a total

Deleted: time of about 20 hours per site

Deleted: sps

Deleted: sps

Deleted: sps

Deleted: or the ability to use

Deleted: stations (too far away compared to wavelengths at 4 kHz) to help suppress local noise, the

Deleted:

Deleted: sps

Next, recorded time series were inspected and trimmed where needed to remove times with spurious noise. The time series were then transformed to the frequency domain and the frequency coefficients of all stations overlapping in time (including the remote reference) were processed with the code of Egbert (1997) to produce robust MT impedances and induction vectors/tippers (Parkinson 1959). The 500 Hz sampling and the recording period of ~1 day allowed reliable responses to be computed within the ~0.01-2000 s range. The use of the Borrego Desert remote reference significantly improved data quality for some sites.

Deleted: sps rate

Deleted:

Following visual inspection of the calculated impedances and tippers, 20% of the impedance data and 16% of the tipper were considered outliers and removed (Fig. 2a). The outliers were generally associated with longest periods (fewer data points per frequency) and southwestern most stations located near the central Coachella Valley where cultural noise was most pronounced (Fig. 2a). This noise affected the electric field recordings more than the magnetic field; thus, tipper data existed at several southwest stations/periods where impedances were otherwise unreliable.

Given the linear nature of the MT array aligned in a southwest-northeast direction where most fault zone structural changes are expected, and the large topographic gradient in the area (22 m to 1495 m), we inverted the responses using the MARE2DEM 2D finite-element algorithm with adaptive meshing that accommodates well irregular topography (Key 2016). Prior to inversion an appropriate strike angle was determined through analyses of the tipper azimuths and phase tensors (Caldwell et al. 2004).

Deleted: a

Deleted: exists

3. Data Analysis

Frequency-dependent phase tensors and tippers provide indicators of the structural characteristics in the area (Figs 2 & S1). Around the Mission Creek strand and shallow depths (<1 s) structure is predominantly 1D, as evidenced by the near circular phase tensors and relatively small tippers. This near surface region probably consists of a shallow layer(s) of damage rock and unconsolidated sediments characteristic of an active fault zone (Blisniuk et al. 2021; Share et al. 2022). After rotating the local coordinate system to the average strike of the Banning and Mission Creek strands (130°/310° E of N, Fig. 1b), the properties of the phase tensor ellipses and tippers show that fault zone geoelectric structures mostly align with fault orientation. At periods ~1-50 s around the Mission Creek strand the phase tensors become elliptical, have <5° beta angles and uniformly align with average fault strike (median strike/alpha=322°, Fig. 2b top). These properties highlight 2D dimensionality at upper to mid crustal depths with geoelectric strike near parallel to average fault strike. This is corroborated by a ~90° flip in beta <5° phase tensor orientations (median strike/alpha=25°, Fig. 2b top) northeast of stations m14-15 (arrow in Figs 1b and 2a), an indication that a prominent fault parallel electric interface has been crossed and the mode with largest phase has flipped from transverse magnetic (TM, southwest conductive side) to transverse electric (TE, northeast resistive side) (Fig. 3). Along the entire profile and for periods up to 50 s, the largest tippers (real part) align with the fault normal (median azimuth=42°/222° E of N, Fig. 2b bottom), further evidence of geoelectric strike approximating fault strike. Moreover, the tippers point (Parkinson convention) toward a region of high conductivity within the SSAF zone (Fig. 2a), most likely related to a fluid-rich region of deformation and damage with the sharp electric contrast around stations m14-15 representing its northeastern edge. At periods >10 s, beta angles start to increase

Deleted: At

Deleted: 50

Deleted: >5° characterize

for impedances recorded in the southwest, which may indicate 3D structure but also reflects the noisy nature of these data. Across the array there is a progressive rotation of phase tensor ellipses and tippers at long periods away from average fault strike (or the fault normal), revealing a deep large-scale 3D plate boundary conductor to the northeast (Fig. S1). This rotation starts at lower periods (~5 s) for northeast stations, highlighting again a resistive region with larger skin depth compared to the conductive fault zone. It also causes a median strike angle of 15° less than the fault normal for stations in the northeast (Fig. 2b top). Taken together, the median of all phase tensor strike (alpha) and real tipper angles up to a period of ~50 s (Fig. 2b) defines a coordinate system with X=311.4° (along fault) and Y=41.4° (across fault). Consequently, the impedances and tippers were rotated and >50 s data excluded from 2D modeling as these express 3D features.

Deleted: .

Deleted: also

Deleted: large

Deleted: contain information about deeper larger-scale

4. 2D Inversion

In pseudosections of the rotated data (Fig. 3a), a broad region of high conductivity encompasses the SSAF zone, with average resistivities to the southwest and highest resistivities beneath stations in the northeast. To properly image the area and delineate SSAF structures, we inverted these data using MARE2DEM. The inversion model space consisted of a ~37 km long surface profile with the Mission Creek strand/Thousand Palms Oasis at Y=0 km (Fig. 4) that included local topography (from Smith & Sandwell 1997) and onto which the 33 station locations were projected. Beyond this 37 km profile, topography was set to be flat and extended from Y=-1,000 km to Y=1,000 km. We fixed the resistivity of the air above the surface to 100,000 Ω.m and beneath the surface the initial value was set to 100 Ω.m. The latter extended down to a depth of 1,000 km. From the surface to ~500 m depth beneath the stations the inversion mesh triangles had a target length of 200 m (see Key (2016) for details). Given the dense station spacing (Fig. 1b) and expected high conductivities of an active fault zone (Fig. 3a), we assigned a target length of 500 m to the mesh from Y=-5 km to +5 km and down to 5 km depth. Outside that zone and down to 10 km depth the target length was 1 km, which then gradually increased to 5 km at 50 km depth and 100 km on either side of the 37 km profile. Beyond that the mesh triangles increased without a specified target length to the edges of the model space.

The impedances and tippers of all except the 5 southwestern most stations were assigned error floors of 10% and 0.02, respectively. To the more 3D and/or noisy data in the southwest (Fig. 2a), we assigned error floors of 15% and 0.03. To test the resolution capabilities of these data plus errors, we constructed synthetic tests using hypothetical fault models, data calculated at the same frequencies and locations as the recorded data, and the same inversion mesh (Fig. S2). The test cases all included a 10 Ω.m 2 km wide fault zone but with attitudes varying from a vertical fault zone to one with a shallow dip of 30° to the northeast (Fig. S2). By keeping the fault zone width and resistivity constant these tests demonstrate the variable lateral and depth resolutions of the data and methodology. The resultant inversions (Fig. S2) after adding Gaussian noise of 10% (impedances) and 0.02 (tippers) to the synthetic data suggest the recorded data are well suited to distinguish between these different fault zone geometries.

Next, MARE2DEM was used to invert the recorded data. A target misfit of rms=1 was set at the start of the inversion and a horizontal to vertical smoothing ratio of 0.5 was selected to highlight expected vertical fault related features (Fig. S2). The MARE2DEM algorithm attempts to reach the target misfit as fast as possible and then afterwards

Deleted: of

Deleted: stations

determines the smoothest model at that misfit (see Key (2016)). The first inversion was run without inverting for the static shifts produced by shallow small-scale features (e.g., structural heterogeneities, sedimentation/groundwater changes, etc.) and irregular topography. After a few iterations (~5) the inversion was stopped to inspect which of the sites may be affected by static shift. These were identified as sites that had low misfits for TE and TM mode phases and TM mode apparent resistivity but had a parallel shift between the TE mode apparent resistivity data and modeled responses. Of the 33 sites, 17 were identified in this manner as having static shifts. Inversion for static shifts was activated for the 17 sites and the inversion restarted with a homogenous 100 Ω.m subsurface. From a starting rms=9.6, the inversion achieved an rms=1.65 after 13 iterations with only incremental improvements after that. Because the initial target of rms=1 was not reached, the model obtained at rms=1.65 was not necessarily the smoothest for that misfit. So, a new target misfit of rms=1.65 was set and the model after 13 iterations was used as the new starting model, and the inversion restarted. After a total of 18 iterations, the smoothest model (Key 2016) with an rms=1.65 was obtained (Fig. 4). The difference between Figs 3a and 3b, and Fig. S3 illustrate how this misfit maps to the different sites and frequencies.

Three crustal resistivity regions characterize this model. First, a complex region of average to high conductivity (minima of ~1 Ω.m at 2 km depth and 12 km depth, C1&C2) exists in the southwest and terminates at a sharp change in resistivity extending from ~2 km northeast of the surface Mission Creek strand to beneath the Banning strand in the ductile crust. The modeled values in this zone are comparable to those of the central San Andreas fault (Bedrosian et al. 2004; Becken et al. 2011). Second, the crust is mostly resistive northeast of this contrast reaching a maximum of ~10,000 Ω.m in places

(R1&R2). Finally, there exists a conductor, separate from C2, at >13 km depth beneath the most elevated part of the Little San Bernardino Mountains in the Joshua Tree National Park (C3). These features' general characteristics do not change with changes in model smoothing or strike of the 2D profile and associated rotations of data responses (Fig. S4).

Given that some regions in the model space are more poorly resolved than others, such as near surface areas with less station coverage, greater depths in general, and regions beneath conductors (e.g., Chave & Jones 2012), we applied a few conductance-preserving (conductivity-thickness product) alterations of particularly C1-C3 to test if small changes in their properties are allowed without significantly affecting the misfit (i.e., changes within the nullspace, Munoz & Rath 2006). MT data are most sensitive to changes in conductance rather than conductivity, so by preserving conductance these tests highlight how changes in the geometries and locations of C1-C3 affect data misfit. They also provide an indication of their relative influence on misfit and, therefore, the relative data sensitivity to these conductive parts of the model space. In general, the tests show that only small changes in C1-C3 are allowed without significantly increasing the model misfit (Fig. 5). Specifically, the steep northeast dipping geometry of anomaly C1 is well resolved as a more vertically orientated structure in the inverted model increases the rms to ~1.8 (Fig. 5). And, the resistive region separating C2 and C3 is similarly well resolved as extensions of either C2 or C3 towards the other lead to large increases in rms (Fig. 5). For example, extending C2 only 6 km to the northeast produces the same significant increase in rms as removing it from the inverted model altogether (Fig. 5).

The model in Fig. 4 is our preferred result as it is equally well constrained by TE, TM and tipper data (Fig. S3) and the majority of that data at periods <50 s is 2D in nature with

Deleted: smaller in scale than and

Deleted: All these features are robust, as their

Deleted: and

Deleted: inversion

Deleted: subsequent rotated

Deleted: Moreover,

Deleted: their locations and shapes

Moved (insertion) [1]

Deleted: Because of the 3D nature of the

Deleted: longer

Deleted: , 3D inversions were carried out a consistent near fault-parallel strike (Fig. 2). However, as noted in Section 3, even at <50 s some stations and periods exhibit 3D characteristics, e.g., at the southwestern and northeastern sites (Fig. 2). As a supplement and to test the effects of these minor 3D features in a predominantly 2D upper to mid crustal region, we additionally applied a 2D determinant inversion (Pedersen & Engels 2005; Wang et al. 2020; 2021). This type of inversion has been shown to produce a less-distorted 2D model representations of a predominantly 2D region that also includes 3D structures (Wang et al. 2020). However, this lower distortion comes at the cost of larger model smoothness. The algorithm employed is embedded in the MARE2DEM package, which facilitates comparison with Fig. 4. During inversion, we used the same impedance tensor data (not tippers), matching errors, and the model and inversion settings described above. Overall, all our resultant determinant inversion models were consistent with Fig. 4. In fact, even when we included data from all available periods, which constituted a significant increase in 3D data, the determinant inversion result was still comparable to Fig. 4 (Fig. S5-S6). In Fig. S5, anomalies C1-3 and R1-2 are all present, albeit the fact that C2 is more conductive and extends to shallower depths, and the region containing R1, R2 and C3 is generally smoother with R1-2 lower in resistivity and C3 smeared towards the northeast where there is less station coverage and the data at longest periods reflect 3D structure (Figs 2 & S1).

As a final reliability test on the inference of a mostly 2D subsurface, a 3D inversion was also carried out using all available data and with the ModEM finite difference code (Kelbert et al. 2014). The features of the 3D model were consistent with our 2D inversions, but lacked the resolution of the MARE2DEM finite element code. These determinant and

Deleted: 2014) to check the reliability of the 2D assumption at shorter periods.

Deleted:

3D inversions demonstrate that our 2D modeling approach applied to a limited dataset is justified and features in the resultant 2D model (Fig. 4) can be reliably interpreted.

5. Discussion

Establishing properties related to structure and strain along the SSAF in Coachella Valley is essential for quantifying the potential magnitude and hazard of future large earthquakes. Fault geometrical irregularities play key roles in rupture propagation and subsequently earthquake magnitudes (e.g., Biasi & Wesnousky 2016). Rupture along dipping faults can produce 2-3 times larger ground shaking in the hanging wall compared to the footwall (Fialko 2006). Strain distributed on several neighboring fault strands instead of a primary fault, influences the likelihood of multi-fault rupture and the extent of the resulting ground motion (Lozos 2016).

The results presented here provide insight into these topics as they relate to the SSAF in the northern Coachella Valley (Fig. 4). Anomaly C1 represents the broad SSAF zone (~3 km wide at the surface) in the upper crust. This near-surface width is corroborated by the present of several anomalous fault damage-related structures within that same ~3 km-wide zone as revealed by analysis of large-N seismic array data (Share et al. 2022). It extends to ~4 km depth with largest amplitude at 2 km and locates northeast of the central Coachella Valley, which implies its vertical to steep northeast dip is fault and not Valley basin controlled (Fig 4). If the Banning and Mission Creek strands predominantly constrain C1's geometry, then they likely have similar vertical to northeast dips at upper crustal depths (Catchings et al. 2009; Chi et al. 2021; Langenheim & Fuis 2021). The emergence of conductor C2 at depths >10 km is attributed to the transition from brittle to ductile

Moved up [1]: 5).

Deleted: This shallow fault zone geometry is well resolved as a more vertically orientated C1 anomaly in the inverted model increases the RMS to ~1.8 (Fig.

behavior in the area (Magistrale 2002; Smith-Konter et al. 2011) and a change in pore-space geometry as deep creep causes minute amounts of migrating fluid to become trapped and highly interconnected (Gough 1986; Park et al. 1992; Wannamaker et al. 2008). These deep fluids are likely sourced from the dehydrating metasediments and/or Peninsular Ranges batholith underlying the Coachella Valley sediments. The modelled location of C2 5-10 km southwest of the surface Mission Creek strand has some uncertainty, because of limited station coverage on that side. In contrast, greater station coverage northeast of the Mission Creek results in lower uncertainty and better model resolution and the data do not require C2 to extend significantly in that direction (Fig. 5). Instead, resistor R1 fits the data best and extends near vertically down to ~20 km depth. The high resistivities of R1 suggest relatively dry hard rock, most likely crystalline basement (Catchings et al. 2009; Ajala et al. 2019), and in case these rocks do contain minor conductive materials, then those materials are not well interconnected and/or exist on such a small scale that they are poorly resolved with the MT frequencies employed. Interestingly, most of the seismicity in this area locates within the more resistive parts of the model (Figs 4 & S5) and is closer to conductor C3 than C1 or C2. We propose C3 is a separate fluid or mineral rich creeping zone in the ductile crust that helps drive local earthquake activity in the more resistive and mechanically stronger crust above it. This correlation between smaller scale brittle failure and high resistivity has been observed along minor faults in central California (Bedrosian et al. 2004) and in Turkey (Gurer & Bayrak 2007).

The uppermost 500 m of C1 has an average resistivity of 35 Ω.m (Fig. 4). Assuming the ~6 Ω.m oases samples are representative of the type of fluids reducing the observed resistivities in the shallow fault zone (they interact and react with similar materials) and

Deleted: . Extending it only 6 km to the northeast produces the same significant increase in RMS as removing C2 from the inverted model altogether (Fig.

Deleted: undetectable

Deleted: R1

Deleted: (R1&R2). The lateral extent of C3 is also well resolved and any attempt to connect it with C2 leads to significant increases in RMS (Fig. 5).

Deleted: also

using Archie's law (Archie 1942), gives porosity estimates of 18% (n=1, highly interconnected crack network) to 44% (n=2, partially connected pores) for the near surface. The further decrease in the resistivity of C1 with depth (minimum of ~1 Ω.m at 2 km depth) can only be explained by decreased fluid resistivities as porosities are expected to decrease with depth also. We suggest two mechanisms driving this. The first is a rapid decrease in fluid resistivity expected in the upper crust due to temperature and pressure increases with depth, which can lead to more than an order of magnitude reduction (Nesbitt 1993). Second, because of the influx of fresh water from the surrounding creeks and mountains, the oases fluids represent an adequate but diluted (more resistive) proxy for the fluids present at 2 km depth in the fault zone. These two factors can result in a reduction of fluid resistivities to <1 Ω.m and produce the observed C1 minimum resistivity if well interconnected cracks with porosities of 10-15% are assumed (e.g., Unsworth et al. 1997; Bedrosian et al. 2004). In the mid-crust porosities decrease even further, the effects of increasing temperature and pressure become negligible (Nesbitt 1993) and observed resistivities are subsequently higher (bottom of C1, Fig. 4). We do not have direct bounds on the conductive material properties producing deeper conductors C2 and C3. Others have suggested that lower crustal conductors in active tectonic settings with resistivities of ~1 Ω.m only require porosities of 0.1-3% if the highly interconnected in situ fluids have salinities close to that of seawater (e.g., Gough 1986; Hyndman et al. 1993; Becken & Ritter 2012). C2 and C3 (at least in part) are likely caused by similar mechanisms.

Taken together, the imaged anomalies and other geophysical inputs permit two interpretations for fault zone geometries and processes (Fig. 4). The major strands of the SSAF zone in the upper crust are vertical to steeply northeast dipping and (1) evolve into

Deleted: evolves

a near vertical fault zone at greater depth that acts mostly as a barrier to northeast migration of fluids sourced in the southwest. A mature fault zone with a well-developed core but diminished damage and deformation zones (i.e., SSAF at mid-crustal depths) is likely to be impermeable (Caine et al. 1996). This type of impermeability and asymmetric distribution of crustal fluids about a major transform fault at depth have been observed along, for example, the central San Andreas and the Dead Sea Transform (Ritter et al. 2003; Bedrosian et al. 2004). Consequently, the seismicity in the northeast is associated with secondary or ancestral faults (Fig. 1a) with small (<5%) associated seismic velocity contrasts (Barak et al. 2015; Share & Ben-Zion 2016; Share et al. 2019). This is in line with the SCEC-CFM5.2 and high-resolution geophysical imaging of the same fault strands but 25 km to the northwest (Catchings et al. 2009). Or (2) the SSAF zone continues to dip northeast at greater depth, accommodates some of the local seismicity, manifests as C3 in the ductile crust but is either dry or consists of disconnected small-scale fluid-rich cracks from ~5 to 13 km depth. These characteristics (2) are not indicative of a mature and active transform fault that has probably experienced many large earthquake ruptures (Weldon et al. 2005). And, it requires an alternate explanation for the imaged near vertical crustal resistivity contrast beneath the surface SSAF zone that is not the active plate boundary. However, (2) is consistent with estimates from geodetic (Fialko 2006; Lindsey & Fialko 2013; Tymofyeyeva et al. 2019) and potential field (Fuis et al. 2012; 2017; Langenheim & Fuis 2021) data, the latter being most sensitive to structures at <10 km depth though.

An argument can be made for a non-simple broad deep SSAF zone that is a mix of (1) and (2), but that would require a lack of kilometer-scale localization of ductile fault roots (e.g., Montési 2013) driven by high crustal temperatures and low viscosities (Takeuchi &

Deleted: around R1

Deleted: to the northeast

Deleted: exceptionally

Deleted: several

Deleted:), and

Deleted: but

Deleted: is

Deleted: within the uppermost 5-

Deleted: Montesi

Fialko 2013). However, heat flow at the site is on par with well-localized fault systems to the north and west (Lachenbruch et al. 1985; Magistrale 2002) and it only starts increasing farther south, as does the observed shallow creep of the SSAF (Sieh & Williams 1990; Tymofyeyeva et al. 2019). Moreover, the deep crustal conductors imaged in this study, inferred to represent ductile fault roots, are not connected but separated by well-resolved resistive crust (Figs 4, 5, S4 & S5).

Deleted: But

Deleted: indeed localized to a few kilometers (Fig. 5

6. Conclusions

Our results permit two interpretations of the electric SSAF zone. It is vertical to steeply northeast dipping in the upper crust and (1) is near vertical at greater depth creating mostly an impermeable barrier for northeast fluid migration or (2) continues to dip northeast but is anomalously dry and relatively resistive up to 13 km depth where it manifests as a secondary deep crustal conductor. We prefer the deeper near vertical fault interpretation (1) as it is the simplest explanation for the active SSAF zone. It is also consistent with other major transform fault systems both in terms of resistivity and its complex shallow to simpler deeper fault zone nature. In any case, the general lack of seismicity and presence of shallow aseismic creep along parts of the Coachella Valley SSAF remain enigmatic. More insights from MT and other geophysical tools are required including joint inversions, which is beyond the scope of this focused study. As a start, we suggest several new across-fault MT arrays in the area. To the southeast these will help establish the along-strike continuity of anomalies C1-C3 and R1, respectively, and delineate changing fault zone widths, geometries, and their connection to seismicity, heat flow and creep. To the northwest more MT data will illuminate the large-scale 3D conductor identified in Figs 2a & S1 and its relation to regional tectonics.

Acknowledgements

We thank Deborah Rogers and Ginny Short (Center for Natural Lands Management and Thousand Palms Oasis Preserve), Brian Ousley (Bureau of Land Management), Tom Anderson, Chris Schoneman and Alicia Thomas (Sonny Bono Salton Sea National Wildlife Refuge), and Martin Alvarez (City of Palm Desert) for help with permitting and access to the field sites. We also acknowledge graduate students Hannah Peterson and Rosslyn King for their assistance during field work. We thank Kerry Key and Gary Egbert for their analysis codes, and Yuri Fialko, Rasheed Ajala and Victoria Langenheim for useful discussions. This work was supported by the Southern California Earthquake Center (SCEC) Award #19200. P.-E. Share was also supported by a Green Foundation Postdoctoral Fellowship (Institute of Geophysics and Planetary Physics/Scripps Institution of Oceanography). S.Wang was funded by the Norwegian Research Council (294404, 309960, and 324442) and the National Infrastructure for High-Performance Computing and Data Storage in Norway (nn9872k).

Deleted: and

Deleted: site

Data Availability

All data are publicly available through ScienceBase (https://doi.org/10.5066/P990U7GE).

Deleted: freely

Deleted: USGS

Formatted: Font: Cambria, Font color: Auto

Formatted: Left, Indent: First line: 0"

References

Ajala, R., Persaud, P., Stock, J. M., Fuis, G. S., Hole, J. A., Goldman, M. R., & Scheirer, D. S. (2019). Three-dimensional basin and fault structure from a detailed seismic velocity model of Coachella Valley, Southern California. Journal of Geophysical Research, 124(5), 4728-4750.

Archie, G. E. (1942). The Electrical Resistivity Log as an Aid in Determining Some Reservoir Characteristics. Transactions of the AIME, 146(01), 54–62. https://doi.org/10.2118/942054-G

Bahr, K. (1997). Electrical anisotropy and conductivity distribution functions of fractal random networks and of the crust: the scale effect of connectivity. Geophysical Journal International, 130, 649-660.

Barak, S., Klemperer, S. L., & Lawrence, J. F. (2015). San Andreas Fault dip, Peninsular Ranges mafic lower crust and partial melt in the Salton Trough, Southern California, from ambient-noise tomography. Geochemistry Geophysics Geosystems, 16, 3946-3972.

Becken, M., & Ritter, O. (2012). Magnetotelluric studies at the San Andreas Fault Zone: Implications for the role of fluids. Surveys in Geophysics, 33(1), 65-105.

Becken, M., Ritter, O., Bedrosian, P. A., & Weckmann, U. (2011). Correlation between deep fluids, tremor and creep along the central San Andreas Fault. Nature, 480(7375), 87-90.

Bedrosian, P. A., Unsworth, M. J., Egbert, G. D., & Thurber, C. H. (2004). Geophysical images of the creeping segment of the San Andreas Fault: implications for the role of crustal fluids in the earthquake process. Tectonophysics, 385, 137-156.

Deleted: ¶

Formatted: Justified

Biasi, G. P., & Wesnousky, S. G. (2016). Steps and Gaps in Ground Ruptures: Empirical Bounds on Rupture Propagation. *Bulletin of the Seismological Society of America*, *106*(3), 1110–1124. https://doi.org/10.1785/0120150175

Blisniuk, K., Scharer, K., Sharp, W. D., Burgmann, R., Amos, C., & Rymer, M. (2021). A revised position for the primary strand of the Pleistocene-Holocene San Andreas fault in southern California. *Science Advances*, *7*(13), eaaz5691. https://doi.org/10.1126/sciadv.aaz5691

Cagniard, L. (1953). Basic theory of the magneto-telluric method of geophysical prospecting. Geophysics, 18, 605-635.

Caine, J.S., Evans, J.P., & Forster, C.B. (1996). Fault zone architecture and permeability structure. Geology 24, 1025–1028.

Caldwell, T. G., Bibby, H. M., & Brown, C. (2004). The magnetotelluric phase tensor. Geophysical Journal International, 158, 457-469.

Carena, S., Suppe, J., & Kao, H. (2004). Lack of continuity of the San Andreas Fault in southern California: Three-dimensional fault models and earthquake scenarios. *Journal of Geophysical Research: Solid Earth*, *109*(B4). https://doi.org/https://doi.org/10.1029/2003JB002643

Catchings, R. D., Rymer, M. J., Goldman, M. R., & Gandhok, G. (2009). San Andreas Fault Geometry at Desert Hot Springs, California, and Its Effects on Earthquake Hazards and Groundwater. *Bulletin of the Seismological Society of America*, *99*(4), 2190–2207. https://doi.org/10.1785/0120080117

Formatted: Justified

Chave, A. D., & Jones, A. G. (Eds.) (2012). *The Magnetotelluric Method: Theory and Practice*. Cambridge University Press. 552 pp.

Chi, B., Qiu, H., Share, P.-E., Vernon, F. L., & Ben-Zion, Y. (2021). Reverse-time migration of fault zone reflected waves: Methodology and application to the Southern San Andreas fault. Seismological Research Letters, 92 (2B), 1422. https://doi.org/10.1785/0220210025

Constable, S. (2013). Review paper: Instrumentation for marine magnetotelluric and controlled source electromagnetic sounding. *Geophysical Prospecting*, *61*(s1), 505–532. https://doi.org/https://doi.org/10.1111/j.1365-2478.2012.01117.x

Egbert, G. D. (1997). Robust multiple-station magnetotelluric data processing. Geophysical Journal International, 130, 475-496.

Fialko, Y. (2006). Interseismic strain accumulation and the earthquake potential on the southern San Andreas fault system. *Nature*, *441*(7096), 968–971. https://doi.org/10.1038/nature04797

Fuis, G. S., Scheirer, D. S., Langenheim, V. E., & Kohler, M. D. (2012). A new perspective on the geometry of the San Andreas fault in southern California and its relationship to lithospheric structure. Bulletin of the Seismological Society of America, 102(1), 236-251.

Fuis, G. S., Bauer, K., Goldman, M. R., Ryberg, T., Langenheim, V. E., Scheirer, D. S., Rymer, M. J., Stock, J. M., Hole, J. A., Catchings, R. D., Graves, R. W., & Aagaard, B. (2017). Subsurface geometry of the San Andreas Fault in Southern California:

585 Results from the Salton Seismic Imaging Project (SSIP) and strong ground motion expectations. Bulletin of the Seismological Society of America, 107(3), 1642-1662.

587 Fumal, T. E., Rymer, M. J., & Seitz, G. G. (2002). Timing of Large Earthquakes since A.D. 800 on the Mission Creek Strand of the San Andreas Fault Zone at Thousand Palms Oasis, near Palm Springs, California. *Bulletin of the Seismological Society of America*, *92*(7), 2841–2860. https://doi.org/10.1785/0120000609

591 Gough, D. I. (1986). Seismic reflectors, conductivity, water and stress in the continental crust. Nature, 323, 143-144.

593 Gurer, A., & Bayrak, M (2007). Relation between electrical resistivity and earthquake generation in the crust of West Anatolia, Turkey. Tectonphysics, 445, 49-65.

595 Hyndman, R. D., Vanyan, L. L., Marquis, G., & Law, L. K. (1993). The origin of electrically conductive lower continental crust: saline water or graphite? Physics of the Earth and Planetary Interiors, 81(1), 325–345.

598 Jones, L. M., Hutton, L. K., Given, D. D., & Allen, C. R. (1986). The North Palm Springs, California, earthquake sequence of July 1986, *Bulletin of the Seismological Society of America*, 76, 1830–1837.

601 Kelbert, A., Meqbel, N., Egbert, G. D., & Tandon, K. (2014). ModEM: A modular system for inversion of electromagnetic geophysical data. Computers & Geosciences, 66, 40–53. https://doi.org/https://doi.org/10.1016/j.cageo.2014.01.010

604 Key, K. (2016). MARE2DEM: a 2-D inversion code for controlled-source electromagnetic and magnetotelluric data. Geophysical Journal International, 207(1), 571-588.

Lachenbruch, A. H., Sass, J. H., & Galanis Jr., S. P. (1985). Heat flow in southernmost California and the origin of the Salton Trough. *Journal of Geophysical Research: Solid Earth*, *90*(B8), 6709–6736. https://doi.org/10.1029/JB090iB08p06709

Langenheim, V. E., & Fuis, G. S. (2022). Insights into the geometry and evolution of the southern San Andreas fault from geophysical data, southern California. *Geosphere*, *18*(2), 458–475.

Lindsey, E. O., & Fialko, Y. (2013). Geodetic slip rates in the southern San Andreas Fault system: Effects of elastic heterogeneity and fault geometry. Journal of Geophysical Research, 118, 689-697.

Lozos, J. C. (2016). A case for historic joint rupture of the San Andreas and San Jacinto faults. Science Advances, 2(3), e1500621.

Magistrale, H., & Sanders, C. (1996), Evidence from precise earthquake hypocenters for segmentation of the San Andreas fault in San Gorgonio Pass, Journal of Geophysical Research, 101, 3031-3044.

Magistrale, H. (2002). Relative contributions of crustal temperature and composition to controlling the depth of earthquakes in Southern California. Geophysical Research Letters, 29(10), 1447.

Montési, L. G. J. (2013). Fabric development as the key for forming ductile shear zones and enabling plate tectonics. *Journal of Structural Geology*, *50*, 254–266.

Muñoz, G., & Rath, V. (2006). Beyond smooth inversion: the use of nullspace projection for the exploration of non-uniqueness in MT. *Geophysical Journal International*, *164*(2), 301–311.

Formatted: Font color: Text 1

Deleted: 2021

Formatted: Font color: Black

Formatted: Font color: Black

Deleted: Southern

Formatted: Font color: Black

Deleted:

Deleted: in press

Formatted: Font: Italic, Font color: Black

Formatted: Font color: Black

Formatted: Font color: Black

Deleted: https://doi.org/https://doi.org/10.1016/j.jsg.2012.12.011 …

Formatted: Not Highlight

Nesbitt, B. E. (1993). Electrical resistivities of crustal fluids. Journal of Geophysical Research, 98(B3), 4301-4310.

Nicholson, C. (1996). Seismic behavior of the southern San Andreas fault zone in the northern Coachella Valley, California: Comparison of the 1948 and 1986 earthquake sequences, *Bulletin of the Seismological Society of America*, 86, 1331–1349.

Nicholson, C., A. Plesch and J.H. Shaw (2017). Community Fault Model Version 5.2: Updating & expanding the CFM 3D fault set and its associated fault database, *2017 SCEC Annual Meeting Proceedings & Abstracts*, XXVII, poster 234, p.142-143.

Ogawa, Y., & Honkura, Y. (2004). Mid-crustal electrical conductors and their correlations to seismicity and deformation at Itoigawa-Shizuoka tectonic line, Central Japan. Earth Planets Space, 56, 1285-1291.

Park, S. K., Jiracek, G. R., & Johnson, K. M. (1992). Magnetotelluric evidence for a brittle-ductile transition, peninsular ranges batholith, southern California? *Geophysical Research Letters*, *19*(21), 2143–2146. https://doi.org/10.1029/92GL02439

Parkinson, W. D. (1959). Directions of rapid geomagnetic fluctuations. Geophysical Journal of the Royal Astronomical Society, 2(1), 1-14.

Pedersen, L. B., & Engels, M. (2005). Routine 2D inversion of magnetotelluric data using the determinant of the impedance tensor. *GEOPHYSICS*, *70*(2), G33–G41.

Ritter, O., Weckmann, U., Hoffmann-Rothe, A., Abueladas, A., Garfunkel, Z., & DESERT Research Group (2003). Geophysical images of the Dead Sea Transform in Jordan reveal an impermeable barrier for fluid flow. Geophysical Research Letters, 30. https://doi.org/10.1029/2003GL017541

Roten, D., Olsen, K. B., Cui, Y. & Day, S. M., 2015. Quantification of fault zone plasticity effects with spontaneous rupture simulations, in *Best Practices in Physics-based Fault Rupture Models for Seismic Hazard Assessment of Nuclear Installations*, Vienna, Austria.

Ross, Z. E., Trugman, D. T., Hauksson, E. & Shearer, P., (2019). Searching for hidden earthquakes in Southern California, Science, 364(6442), 767-771.

Rymer, M. J. (2000). Triggered Surface Slips in the Coachella Valley Area Associated with the 1992 Joshua Tree and Landers, California, Earthquakes. *Bulletin of the Seismological Society of America*, *90*(4), 832–848. https://doi.org/10.1785/0119980130

Schwarz, G. (1990). Electrical conductivity of the earth's crust and upper mantle. Surveys in Geophysics, 11, 133-161.

Share, P.-E., & Ben-Zion, Y. (2016). Bimaterial interfaces in the South San Andreas Fault with opposite velocity contrasts NW and SE from San Gorgonio Pass. Geophysical Research Letters, 43(20), 10680-10687.

Share, P.-E., Guo, H., Thurber, C. H., Zhang, H. & Ben-Zion, Y., 2019. Seismic imaging of the Southern California plate-boundary around the South-Central Transverse Ranges using double-difference tomography, Pure and Applied Geophysics, 176(3), 1117-1143.

Share, P., Qiu, H., Vernon, F. L., Allam, A. A., Fialko, Y., & Ben-Zion, Y. (2022). General Seismic Architecture of the Southern San Andreas Fault Zone around the Thousand Palms Oasis from a Large-N Nodal Array. *The Seismic Record*, *2*(1), 50–58.

Formatted: Font color: Custom Color(RGB(26,26,26))

Sieh, K., & Williams, P. (1990). Behavior of the southernmost San Andreas fault during the past 300 years. *Journal of Geophysical Research*, 95, 6629–6645.

Smith, W. H. F., & Sandwell, D. T. (1997). Global seafloor topography from satellite altimetry and ship depth soundings. *Science*, 277, 1957–1962.

Smith-Konter, B. R., Sandwell, D. T., & Shearer, P. (2011). Locking depths estimated from geodesy and seismology along the San Andreas Fault System: Implication for seismic moment release. Journal of Geophysical Research, 116, B06401.

Takeuchi, C. S., & Fialko, Y. (2013). On the effects of thermally weakened ductile shear zones on postseismic deformation. *Journal of Geophysical Research: Solid Earth*, *118*(12), 6295–6310. https://doi.org/https://doi.org/10.1002/2013JB010215

Tietze, K., & Ritter, O. (2013). Three-dimensional magnetotelluric inversion in practice—the electrical conductivity structure of the San Andreas Fault in Central California. *Geophysical Journal International*, *195*(1), 130–147. https://doi.org/10.1093/gji/ggt234

Turkoglu, E., Unsworth, M., Caglar, I., Tuncer, V., & Avsar, U. (2008). Lithospheric structure of the Arabia-Eurasia collision zone in eastern Anatolia: magnetotelluric evidence for widespread weakening by fluids? Geology, 36, 619-622.

Tymofyeyeva, E., Fialko, Y., Jiang, J., Xu, X., Sandwell, D., Bilham, R., Rockwell, T. K., Blanton, C., Burkett, F., Gontz, A., & Moafipoor, S. (2019). Slow slip event on the southern San Andreas fault triggered by the 2017 M_W8.2 Chiapas (Mexico) earthquake. *Journal of Geophysical Research*, 124, B016765.

Formatted: Justified

Unsworth, M. J., Malin, P. E., Egbert, G. D., & Booker, J. R. (1997). Internal structure of the San Andreas fault at Parkfield, California. Geology, 25(4), 359–362.

Wang, S., Constable, S., Reyes-Ortega, V, Jahandari, H., Farquharson, C., & Avile-Esquivel, T. (2020). Two-dimensional determinant inversion of marine magnetotelluric data and a field example from the Gulf of California, Mexico. *Geophysics*, 86, E37–E57.

Wang, S., Constable, S., Rychert, C. A., & Harmon, N. (2021). A lithosphere-asthenosphere boundary and partial melt resolved using marine magnetotelluric data, *Geochemistry Geophysics Geosystems,* 21, doi.org/10.1029/2020GC009177

Wannamaker, P. E., Hasterok, D. P., Johnston, J. M., Stodt, J. A., Hall, D. B., Sodergren, T. L., Pellerin, L., Maris, V., Doerner, W. M., Groenewold, K. A., & Unsworth, M. J. (2008). Lithospheric dismemberment and magmatic processes of the Great Basin-Colorado Plateau transition, Utah, implied from magnetotellurics, Geosystems Geophysics Geochemistry, 9, Q05019.

Weldon, R. J., Fumal, T. E., Biasi, G. P., Scharer, K. M. (2005). Past and future earthquakes on the San Andreas fault, Science, 308, 966-967.

Yoshimura, R., Oshiman, N., Uyeshima, M., Toh, H., Uto, T., Kanezaki, H., Mochido, Y., Aizawa, K., Ogawa, Y., Nishitani, T., Sakanaka, S., Mishina, M., Satoh, H., Goto, T., Kasaya, T., Yamaguchi, S., Murakami, H., Mogi, T., Yamaya, Y., Harada, M., Shiozaki, I., Honkura, Y., Koyama, S., Nakao, S., Wada, Y., & Fujita, Y. (2009). Magnetotelluric transect across the niigata-kobe tectonic zone, central Japan: a clear

Formatted: Font: Times New Roman

correlation between strain accumulation and resistivity structure. Geophysical Research Letters, 36, L20311.

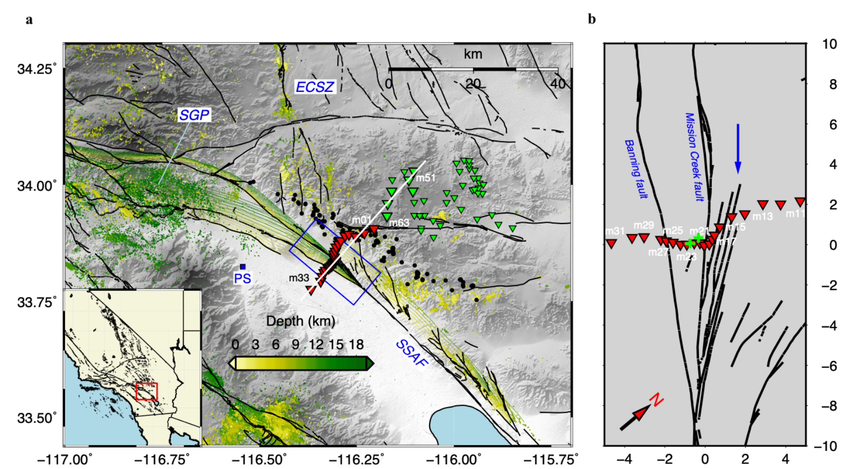

Figure 1: Study area in the context of the Southern San Andreas Fault (SSAF). (a) Fault traces at the surface (black lines) and contours along the SSAF planes from shallow (yellow) to 14 km depth (green) from the SCEC-CFM5.2 (see text). The SSAF strand accommodating most of the plate boundary strain to the south is estimated to be vertical and has no contours. Secondary or ancestral faults are associated with the dipping structures (contours) to the northeast. Magnetotelluric (MT) stations acquired in 2019 (red) and in the Joshua Tree National Park during 2017-2018 (green) are depicted by triangles. Larger triangles show stations used in the 2D inversion and the white line represents the inversion model transect in Fig. 4. Depth colored dots are local earthquakes from the Ross et al. (2019) catalog. Black dots are events illuminating a large bimaterial structure at depth. Note the relative lack of seismicity directly beneath the SSAF and especially near the study area.

Deleted: ¶
¶
¶
a)

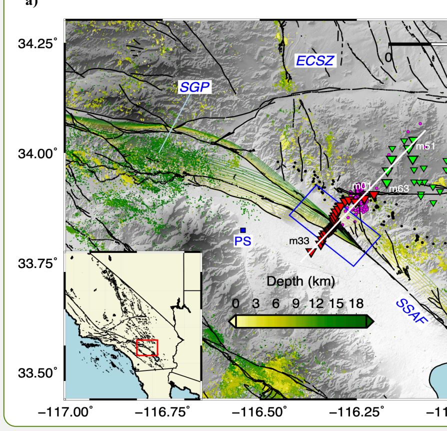

Deleted: and the magenta circles correspond to those plotted in Fig. 4

San Gorgonio Pass (SGP), the Eastern California Shear Zone (ECSZ) and the town of Palm Springs (PS) are shown for reference. (b) Zoom in of blue box in (a) showing the MT profile transecting the SSAF zone, which consists of the Banning, Mission Creek, and other minor fault strands. The blue arrow shows the location of a large change in electric resistivity in the across-fault direction (same arrow appears in Figs 2-4). The Thousand Palms Oasis Preserve Visitor Center is located at the origin and the green crosses show the locations of two fluid samples taken from the oases.

Deleted: , 3 &

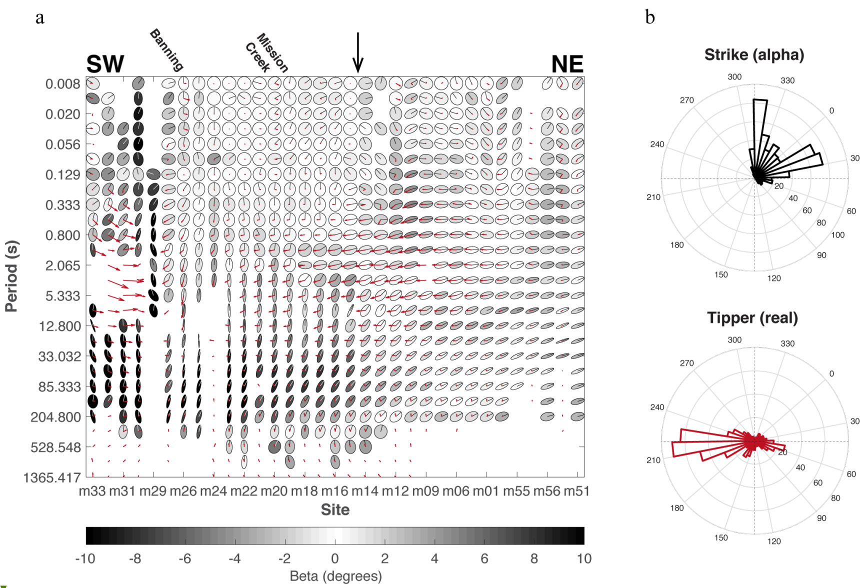

Deleted:

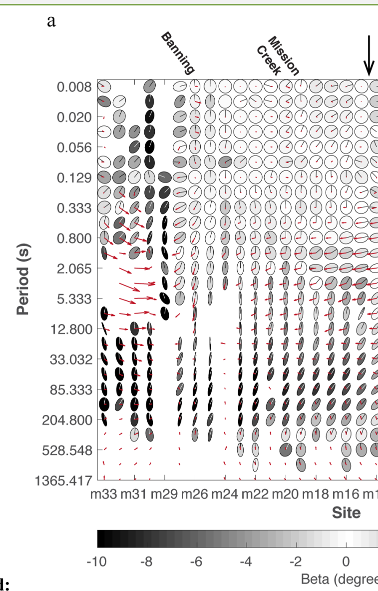

Figure 2: Phase tensor and tipper results. (a) Phase tensor ellipses and real tipper vectors (maroon arrows, Parkinson convention) of all data after outliers (gaps) were removed. The degree of ellipticity equals the difference between Phi-min and Phi-max, the black lines inside ellipses point to calculated strike (alpha) and the orientation of the major axes of ellipses relative to strike and the shading of the ellipses equals beta. The coordinate frame is the same as in Fig. 1b. (b) Histograms of strike (top) and real tipper azimuths (bottom) for data up to 50 s. The dashed lines show the coordinate frame used (same as in (a)).

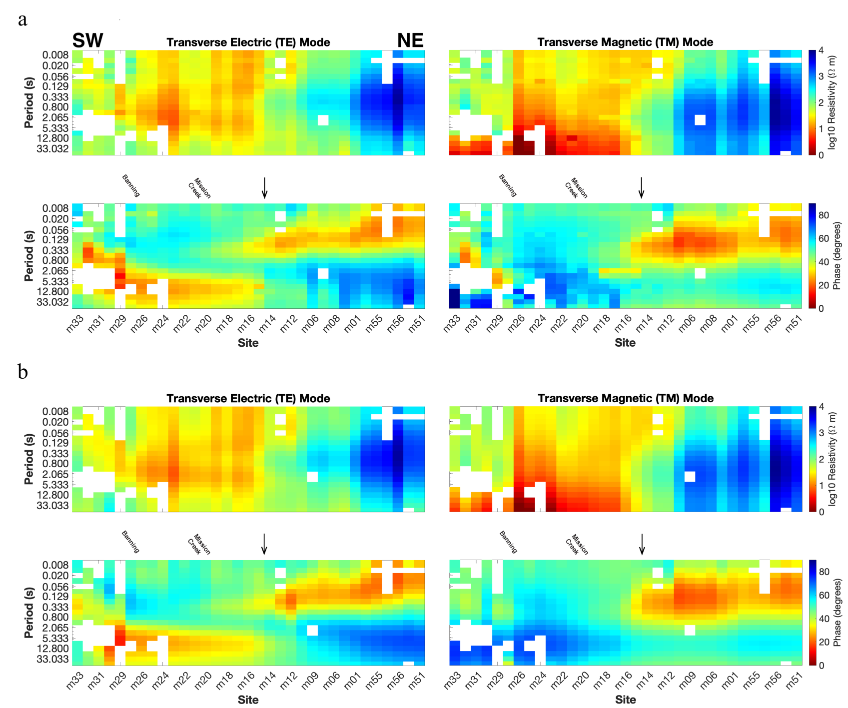

Figure 3: Pseudosections for the TE (left) and TM (right) modes up to 50 s period associated with recorded (a) and modeled (b) data responses. The modeled data correspond to the inverted model in Fig. 4. Differences between (a) and (b) are also illustrated in Fig. S3.

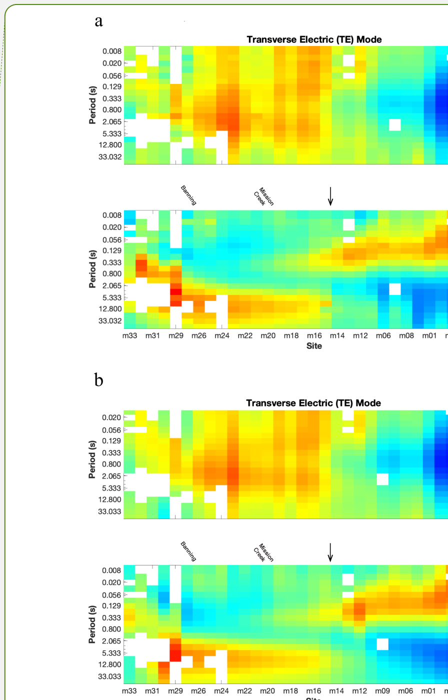

Deleted:

Deleted: and

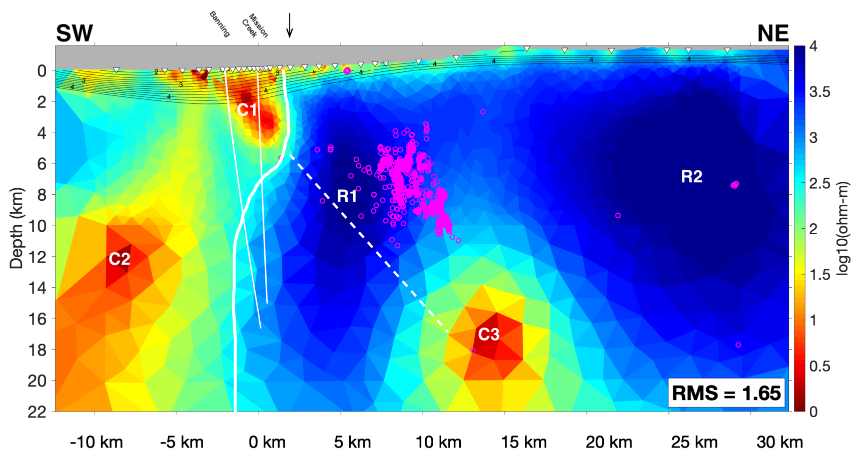

Deleted: 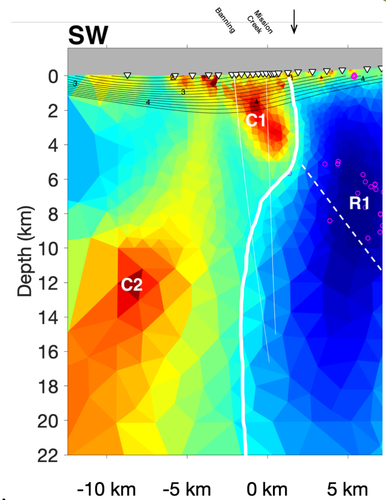

Figure 4: Final 2D inverted model with prominent conductors (C1-C3) and resistors (R1-R2) marked. Magenta circles are local earthquakes within 3 km of this 2D plane. The thick white line highlights a region of sharp resistivity change throughout the crust and represents one (and the preferred) interpretation for the location of the northeastern edge of the shallow SSAF zone and its near vertical geometry at greater depth. The nearby thinner white lines depict geometries of the Banning and Mission Creek strands from the SCEC-CFM5.2 (Fig. 1a). The dashed white line connecting C1 and C3 is an alternate interpretation of SSAF zone geometry at greater depth. Black contours are from the P-wave velocity model of Ajala et al. (2019) from 2 km/s to 4.4 km/s sampled at increments of 0.2 km/s and highlights mostly basin geometry in the central Coachella Valley.

Deleted: (Fig. 1a).

Deleted: thin

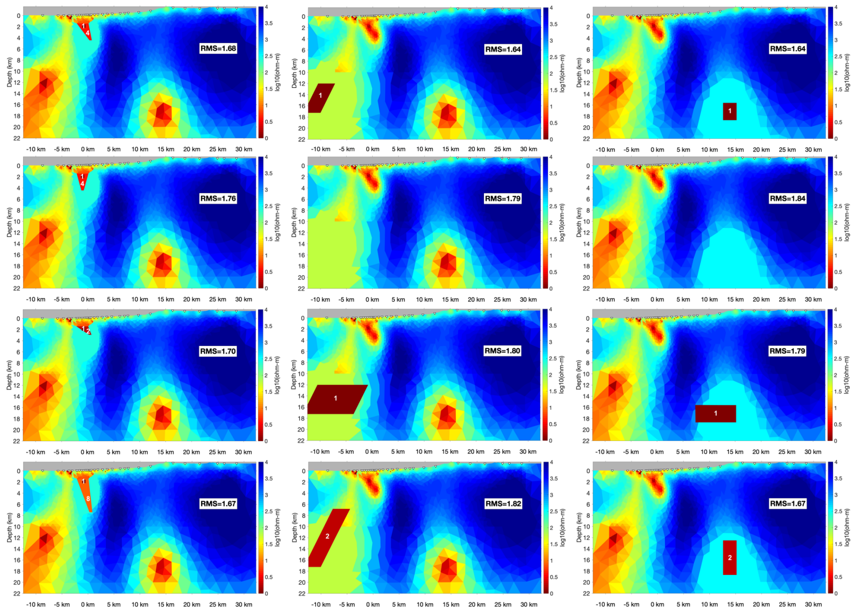

Figure 5: Equivalent resistivity anomaly representations of conductors C1 (left column), C2 (middle column) and C3 (right column) with similar misfits as in Fig. 4 (top row). Lower panels show removals, extensions and translations of these anomalies (all subsequent rows), and, the misfits associated with those alterations. Numbers inside anomalies represent resistivities in Ω.m.

Deleted: the removals and conductance-preserving (conductance = electrical conductivity x thickness)

Dear Editor,

We would like to submit a revised version of the manuscript entitled "**Structural properties of the Southern San Andreas fault zone in northern Coachella Valley from magnetotelluric imaging**" for publication in *Geophysical Journal International*.

This concise paper provides, for the first time, relatively high-resolution electromagnetic imaging results of the Southern San Andreas fault (SSAF) zone using a dense across-fault magnetotelluric (MT) array. MT is a non-seismic tool here applied to an anomalously aseismic and therefore poorly informed major fault system (i.e., SSAF) that is also one of the largest seismic hazards and risks in Southern California. In general, MT is a largely underutilized geophysical method in Southern California and this study therefore provides a seed for many future works in the area using similar tools.

The imaged fault associated conductors and resistors reveal crustal fluids (or the lack thereof) within shallow brittle damaged structures and highly interconnected minute amounts of fluids in ductile fault roots beneath the SSAF. Taken together, these features most likely suggest a near vertical San Andreas fault zone in the northern Coachella Valley and more distributed deformation in the ductile crust than reported in previous studies. These results help answer several outstanding questions about local fault structure and may help consolidate some of the competing views between different geoscientific fields as it relates to properties of the SSAF.

The paper has various figures that should be in color online and in print.

The first author of the paper was a postdoctoral researcher at the time of this project (now an assistant professor). He took the lead on all the analyses performed in the study, as well as on writing the results.

Yours sincerely,

Pieter-Ewald Share for all authors